UCSB-HEP-96-01
HUTP-96/A023
To be published in Reviews of Modern Physics

The discovery of the top quark

Claudio Campagnari

University of California, Santa Barbara, California 93106

Melissa Franklin

Harvard University, Cambridge, Massachussets 02138

Abstract

Evidence for pair production of a new particle consistent with the Standard Model top quark has been reported recently by groups studying proton anti-proton collisions at 1.8 TeV center of mass energy at the Fermi National Accelerator Laboratory. In this paper we review the history of the search for the top quark in electron positron and proton anti-proton collisions. We report on a number of precise electro-weak measurements and the value of the top quark mass which can be extracted from these measurements within the context of the Standard Model. We review the theoretical predictions for top quark production and the dominant backgrounds. We describe the collider and the detectors that were used to measure the pair production process and follow on to describe the data from which the existence of the top quark is evinced. Finally, we present possible measurements that could be made in the future with more data, measurements of quantities that would confirm the nature of this particle, the details of its production in hadron collisions, and its decay properties.

CONTENTS

I. INTRODUCTION

The intensive experimental efforts in the search for the heaviest fundamental fermion culminated in 1995 with the discovery of the top quark in proton-antiproton annhilations at the Fermilab Tevatron Collider. Observation of the top quark is the latest in a long series of triumphs for the Standard Model of particles and fields. The top quark is the last fundamental fermion and the next-to-last fundamental particle predicted by the Standard Model. Only the Higgs boson remains unobserved.

The search for the top quark started in the late seventies, soon after discovery of the companion bottom-quark. It has been a long and arduous process because the top quark turned out to be much more massive than was originally expected. The mass of the top quark is remarkably large, approximately 200 times larger than the mass of the proton and 40 times higher than the mass of the next lightest quark. Whether this property of the top quark is a mere accident or a manifestation of a deeper physical process is an unanswered question in particle physics.

The discovery of the top quark has been made possible by the technological progresses in high energy physics in the past fifteen years. In particular, the development of proton-antiproton colliders, pioneered first at CERN and then at Fermilab has been a crucial ingredient in the discovery of the top.

In this article we review the discovery of the top quark as well as the developments that led to it. In Section II we discuss the top quark within the framework of the Standard Model. While the top quark mass is a free parameter in the Standard Model, its value enters in calculations of a number of electroweak observables. The top-mass dependence of the theoretical predictions is in general rather weak. However, the accuracy of many of these measurements is now such that meaningful constraints on the top quark mass can be obtained by comparing them with theoretical predictions. These constraints constitute a test of the predictive power of the Standard Model, and are reviewed in Section III. The top production mechanisms in proton-antiproton collisions, and the experimental signatures of top events that are crucial to the understanding of the experimental results are discussed in Section IV and V. Early searches for the top quark are described in Section VI. The Tevatron Collider, whose remarkable performance played a very important role in the discovery of the top quark, will be described briefly in Section VII. The data that finally led to the discovery of the top quark are reviewed in Section VIII. The value of the top mass is of fundamental importance, and it is needed to complete precise tests of the Standard Model. Furthermore, from an experimental point of view, the techniques developed to measure the top mass are new and particularly interesting. The top mass measurement is described in Section IX. Historically, discoveries of new leptons or quarks have opened up new fields of inquiry which have enhanced our understanding of elementary particles and their interactions. Consequently, this article concludes in Section X with a discussion of the experimental prospects for top physics.

II. THE ROLE OF THE TOP QUARK IN THE STANDARD MODEL

Quarks and leptons constitute the basic building blocks of matter in the Standard Model (SM). There are three *generations* of quarks and leptons in the model, with identical quantum numbers, but different masses. Within each generation, quarks and leptons appear in pairs, (see Fig. 1). The left-handed quarks form weak isospin doublets, with the Q= +2/3 and Q= −1/3 quarks having weak isospin $I_3 = +1/2$ and $-1/2$ respectively.

Quarks

			I_3	Y	$Q = I_3 + Y/2$
$\begin{bmatrix} u \\ d \end{bmatrix}_L$	$\begin{bmatrix} c \\ s \end{bmatrix}_L$	$\begin{bmatrix} t \\ b \end{bmatrix}_L$	$+1/2$ $-1/2$	$+1/3$ $+1/3$	$+2/3$ $-1/3$
u_R	c_R	t_R	0	$+4/3$	$+2/3$
d_R	s_R	b_R	0	$-2/3$	$-1/3$

Leptons

$\begin{bmatrix} \nu_e \\ e \end{bmatrix}_L$	$\begin{bmatrix} \nu_\mu \\ \mu \end{bmatrix}_L$	$\begin{bmatrix} \nu_\tau \\ \tau \end{bmatrix}_L$	$+1/2$ $-1/2$	-1 -1	0 -1
e_R	μ_R	τ_R	0	-2	-1

FIG. 1. Leptons and quarks in SU(2)xU(1) (Standard Model). Also shown are the values for the SU(2) weak isospin (I_3), U(1) weak hypercharge (Y), and electric charge (Q, in units of the electron charge). The subscripts L and R refer to the left and right-handed components respectively.

The tau-lepton (τ) was the first particle of the third generation to be discovered (Perl *et al.*, 1975). A short time later, in 1977, the Υ was discovered at Fermilab (Herb *et al.*, 1977) as a resonance in the $\mu^+\mu^-$ invariant mass spectrum in the reaction p + nucleon $\rightarrow \mu^+\mu^- +$ X. This resonance was interpreted as a $b\bar{b}$ bound state (the Υ), which subsequently decays into muon pairs. As will become abundantly clear in the remainder of this paper, the top signature in hadron collisions is much more complicated.

In the past fifteen years, a tremendous amount of experimental data on the properties of the b-quark and of b-flavored hadrons have become available, mostly from experiments at e^+e^- colliders. Both the charge and the weak isospin of the bottom-quark are by now well established ($Q_b = -1/3$, and $I_3 = -1/2$).

The value of the charge was first inferred from measurements of the Υ leptonic width (Berger *et al.*, 1978; Darden *et al.*, 1978; Bienlein *et al.*, 1978) at the DORIS e^+e^- storage

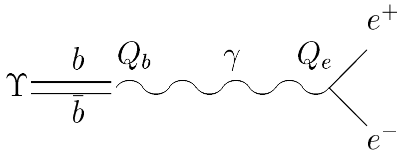

FIG. 2. Feynman diagram for $\Upsilon \rightarrow e^+e^-$.

Model 1	Model 2	Model 3	Experimental value
1.05 keV	1.07 keV	1.15 $\pm$ 0.20 keV	1.22 $\pm$ 0.03 keV

TABLE I. The experimental value of $\Gamma(\Upsilon \rightarrow e^+e^-)$ compared with theoretical expectations from quark-antiquark potential models assuming $Q_b = -1/3$. Model 1 : Krasemann and Ono, 1979. Model 2 : Büchmuller, Grunberg and Tye, 1980. Model 3 : Voloshin and Zakharov, 1980. The quoted experimental value is from the compilation of the Particle Data Group, corrected by 7 % for consistency in comparison with potential model calculations, which only include the lowest order Born term (Montanet *et al.*, 1994).

ring. This width is proportional to the square of the charge of the b-quark, (see Fig. 2), and can be quantitatively estimated from heavy quark-antiquark potential models, see Table I (Quigg and Rosner, 1977; Eichten and Gottfried, 1977; Rosner, Quigg, and Thacker, 1978; Krasemann and Ono, 1979; Büchmuller, Grunberg and Tye, 1980; Voloshin and Zakharov, 1980). The charge assignment was subsequently confirmed by measurements of R $= \sigma(e^+e^- \rightarrow \text{hadrons}) / \sigma(e^+e^- \rightarrow \mu^+\mu^-)$. At lowest order, and ignoring resonance effects, R $= \sum_{quarks} 3Q_q^2$, where the factor of three arises from the fact that quarks come in three colors. The sum is over all quarks that can be produced, i.e. all quarks with mass below one-half the center of mass energy of the e^+e^- system. Above threshold for $b\bar{b}$ production, the value of R was found to increase by $0.36 \pm 0.09 \pm 0.03$ (Rice *et al.*, 1982), in agreement with the expectations of $3Q_b^2$=1/3. The pole mass of the b-quark is estimated to be in the range 4.5 - 4.9 GeV/c^2 from knowledge of the Υ and b-meson masses (Montanet *et al.*, 1994).

The weak isospin of the b-quark was first extracted from the forward-backward asymmetry (A_{FB}) in $e^+e^- \rightarrow b\bar{b}$. This asymmetry is defined in terms of the b-quark production cross section $\sigma(b)$ as

$$A_{FB} = \frac{\sigma(b, \theta > 90^o) - \sigma(b, \theta < 90^o)}{\sigma(b, \theta > 90^o) + \sigma(b, \theta < 90^o)}$$

where θ is the polar angle of the b-quark in the e^+e^- center of mass as measured from the direction of flight of the e^-. The asymmetry originates from the coupling of the Z to fermions, which in the Standard Model depends on the weak isospin through a term in the lagrangian of the form $\bar{f}\gamma_\mu(g_V - g_A\gamma_5)Z^\mu f$, where the vector and axial couplings g_V and g_a are given by

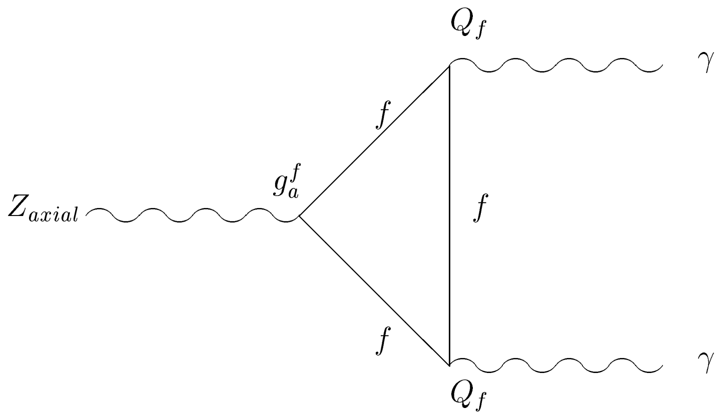

FIG. 3. An example of a fermion triangle diagram which could cause an anomaly; g_a^f is the fermion axial coupling to the Z, and Q_f is the fermion charge.

$$g_V = \frac{I_3 - 2Q\sin^2\theta_W}{2\sin\theta_W\cos\theta_W}$$
$$g_A = \frac{I_3}{2\sin\theta_W\cos\theta_W}$$

and θ_W is the Weinberg angle. The first measurement of A_{FB} was performed in the mid-eighties ($A_{FB} = -22.8\pm6.0\pm2.5\%$ at $\sqrt{s} = 34.6$ GeV; Bartel *et al.*, 1984), and was found to be consistent with the Standard Model prediction ($A_{FB} = -25\%$) assuming $I_3 = -1/2$ for the weak isospin of the *b*-quark. Alternative isospin assignments (e.g. I=0) for the bottom-quark were also found to be inconsistent with the observed suppression of flavor-changing neutral current decays of *b*-mesons. If the *b*-quark formed a weak-isospin singlet, and if there were only five quarks (u, d, c, s, b), then it can be shown that $BR(B\rightarrow Xl^+l^-) \geq 0.12$ $BR(B\rightarrow Xl\nu) \approx 0.026$ (Kane and Peskin, 1982). This was soon found to be inconsistent with the first upper limits placed on flavor changing neutral currents in *b*-decays, $BR(B\rightarrow Xl^+l^-)$ < 0.008 at 90% C.L. (Matteuzzi *et al.*, 1983).

The $I_3 = -1/2$ isospin of the bottom quark implies the existence of an additional quark, the top quark, as the third-generation weak isospin partner of the bottom quark. Furthermore, the existence of such a third generation quark doublet, in conjunction with the presence of three lepton generations, ensures the necessary cancellations in diagrams contributing to triangle anomalies. For the electro-weak theory to be renormalizable, the sum over fermions for diagrams such as the one displayed in Fig. 3 should vanish (see for example Leader and Pedrazzi, 1982). The contributions to this diagram for each fermion in the theory is proportional to $N_c g_a^f Q_f^2$, where the factor $N_c = 3$ is the number of colors and applies to quarks only. Hence, the contribution from a lepton isodoublet exactly cancels that of a quark isodoublet. With three lepton generations, the existence of a third quark isodoublet, whose members are the top and bottom quarks, results in the desired cancellation of triangle anomalies.

Measurements of the Z width at the LEP and SLC colliders rule out the existence of a 4th generation neutrino with mass $M_\nu \lesssim M_Z/2$ (Montanet *et al.*, 1994). Unless the 4th generation neutrino is very massive, no additional generations are allowed in the context of the Standard Model. The top quark is therefore the last fermion expected in the Standard Model. Only the Higgs boson is left to be discovered in order to complete the particle and field content of the minimal Standard Model.

While the Standard Model predicts the charge and weak isospin of the top quark ($Q = 2/3$, and $I_3 = 1/2$), its mass remains a free parameter. As we will discuss in Section IX, the recent top mass measurements yield $M_{top} = 175 \pm 8$ GeV/c^2, a factor of 40 higher than the mass of the second heaviest fundamental fermion (the b-quark). The reason for such a high mass for the top quark is a mystery of the Standard Model. It does however occur quite naturally in local supersymmetric theories where the electro-weak symmetry is broken through radiative corrections (Ibanez and Lopez, 1983; J. Ellis *et al.*, 1983; Alvarez-Gaume, Polchinski, and Wise, 1983).

The value of the top mass enters in the calculation of radiative corrections to a large number of electro-weak observables. As we will discuss in Section III, the level of precision achieved in these measurements is good enough that a comparison between the measured top mass and the calculation of electro-weak radiative corrections provides a stringent test of electro-weak theory and is sensitive to physics beyond the Standard Model.

III. TOP MASS AND PRECISION ELECTRO-WEAK MEASUREMENTS

Over the past few years, a number of very precise measurements at e^+e^- colliders have been performed using large samples of Z events. At CERN the four LEP experiments (Aleph, Delphi, L3, and Opal) have collected of order two million Z events each, and at the SLC collider at SLAC the SLD experiment has collected a data sample of order one hundred thousand events. Although the SLAC data sample is considerably smaller than the LEP data sample, it was possible to polarize the beams at the SLC and this lead to a competitive measurement of the Weinberg angle. The level of accuracy of the LEP and SLC measurements, as well as of measurements of the W-boson mass at the Tevatron, is now such that the data are not well described by tree-level theoretical calculations and radiative corrections must be included.

If we assume that the Standard Model can be used to correctly calculate higher order electro-weak processes, we can infer the top quark mass by comparing these calculations to precise measurements (Altarelli, Kleiss, and Verzegnassi, 1989). We can then check whether this value is consistent with the directly measured top quark mass. The free parameters in the model are the weak coupling constant G_{Fermi}, the electromagnetic coupling constant α, the Weinberg angle, θ_W, the mass of the Higgs boson, M_{Higgs}, the strong coupling constant α_s, the masses of the six quarks, the masses of the six leptons, and the four quark mixing parameters which determine the CKM matrix.

At lowest order the masses of the weak intermediate vector bosons can be determined completely from the first three of these parameters, G_{Fermi}, α, and θ_W. The best measured Standard Model parameters are α, G_{Fermi} and M_Z. Using these three parameters we can, at lowest order predict several measurable quantites. However, when higher order corrections are considered, the fermions and Higgs masses enter into the calculations. The top mass plays a particularly large role in these radiative corrections due to the large mass difference beween the top quark and its weak isospin partner, the bottom quark. The dependence of these radiative corrections on the top quark mass contains terms quadratic in M_{top} of the form M_{top}^2/M_Z^2, whereas the Higgs mass dependence is logarithmic ($\ln(M_{Higgs}/M_Z)$). Fig. 4

shows two higher order diagrams involving top quark and Higgs radiative corrections which modify observables at the Z resonance.

A. Neutral current experiment measurments

At LEP and SLC, the line shape and asymmetries at the Z have been precisely measured and can be compared with theoretical prediction. The uncertainties on most of these quantities are smaller from the LEP measurements due to the size of the LEP data samples. These quantities are:

- The total width of the Z, Γ_Z.
- The value of the hadronic cross section at the Z peak, $\sigma^0_{had} \equiv \frac{12\pi}{m_Z^2}\frac{\Gamma_{ee}\Gamma_{had}}{\Gamma_Z^2}$.
- The ratio of the hadronic to leptonic widths, $R_l \equiv \Gamma_{had}/\Gamma_{ll}$.
- The forward-backward asymmetry in $Z \to ll$ decays, $A^{0,l}_{FB} \equiv \frac{3}{4}A_e A_f$ where $A_f \equiv \frac{2g_{Vf}g_{Af}}{g^2_{Vf}+g^2_{Af}}$, and the leptons ($l$) include e, μ and τ.
- A_τ as defined above. This is obtained from measurements of the τ polarization defined as $P_\tau \equiv \frac{\sigma_R-\sigma_L}{\sigma_R+\sigma_L}$ where σ_R and σ_L are the τ pair cross sections for the production of right and left-handed τ's respectively.
- A_e, as defined above, i.e. $A_e \equiv \frac{2g_{Ve}g_{Ae}}{g^2_{Ve}+g^2_{Ae}}$.
- The forward-backward asymmetry for decays, $Z \to b\bar{b}$ and $Z \to c\bar{c}$, at the Z pole mass, $A^{0,b}_{FB}$ and $A^{0,c}_{FB}$.
- The value of $\sin^2\theta^{lept}_{eff} \equiv \frac{1}{4}(1 - \frac{g_{Vl}}{g_{Al}})$ from the hadronic charge asymmetry, $< Q_{FB} >$ which is the forward-backward asymmetry measured from $Z \to q\bar{q}$ decays. The charge of the outgoing quark is determined using a statistical weighting method.
- The ratios $R_b \equiv \frac{\Gamma_Z^{b\bar{b}}}{\Gamma_Z^{hadrons}}$ and $R_c \equiv \frac{\Gamma_Z^{c\bar{c}}}{\Gamma_Z^{hadrons}}$.
- The left-right asymmetry, $\mathrm{A}_{LR} \equiv (\sigma_L - \sigma_R)/(\sigma_L + \sigma_R)$, where σ_L and σ_R are the production cross sections for Z bosons at the Z pole energy with left-handed and right-handed electrons respectively. This measurement has been performed only at the SLC, since the beams are unpolarized at LEP.

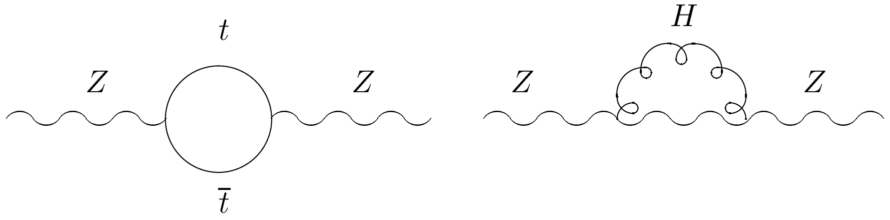

FIG. 4. Examples of radiative corrections to the Z mass involving top quarks or Higgs boson loops.

In Fig. 5 and Fig. 6 we show the measurements of the variables listed above at LEP (The LEP Collaborations, 1995), compared with Standard Model expectations as a function of the top quark mass. The vertical bands are the measurements, where the width of the bands include one standard deviation uncertainties. The cross-hatched bands show the theoretical predictions taking into account the uncertainty on the Higgs mass (the inner bands) and the uncertainty on the value of the strong coupling constant α_s (the outer bands). In calculating the theoretical uncertainties, the Higgs mass is varied from 60 to 1000 GeV/c^2 and α_s is varied within the interval $\alpha_s(M_z^2) = 0.123 \pm 0.006$ (Bethke, 1995). The dependence of the Z width measurements on α_s enters through radiative diagrams involving gluons, an example of which is shown in Fig. 7. The LEP measurements are consistent with theoretical predictions, except for the ratios R$_b$ and R$_c$, which will be discussed in Section III.A.2.

1. Asymmetries at the Z

The asymmetries measured at LEP, $A_{FB}^{0,l}$, A_τ, A_e, $A_{FB}^{0,b}$, $A_{FB}^{0,c}$ and $< Q_{FB} >$ are effectively measurements of $\sin^2\theta_{eff}^{lept}$. Despite the lower statistics SLC Z sample, the A$_{LR}$ measurement from SLD provides a competitive measurement of $\sin^2\theta_{eff}^{lept}$. $\sin^2\theta_{eff}^{lept}$ has also been measured in νN experiments at lower center of mass energies (Abramowicz *et al.*, 1986; Blondel *et al.*, 1990; Allaby *et al.*, 1986 and 1987; Arroyo *et al.*, 1994). All of these measurements of $\sin^2\theta_{eff}^{lept}$ are found to be consistent within their respective uncertainties and are combined. The combined result from LEP is $\sin^2\theta_{eff}^{lept} = 0.23186 \pm 0.00034$, while the corresponding result from the SLD A$_{LR}$ measurement is $\sin^2\theta_{eff}^{lept} = 0.23049 \pm 0.00050$ (Woods, 1996). Figure 8 summarizes all the measurements of $\sin^2\theta_{eff}^{lept}$.

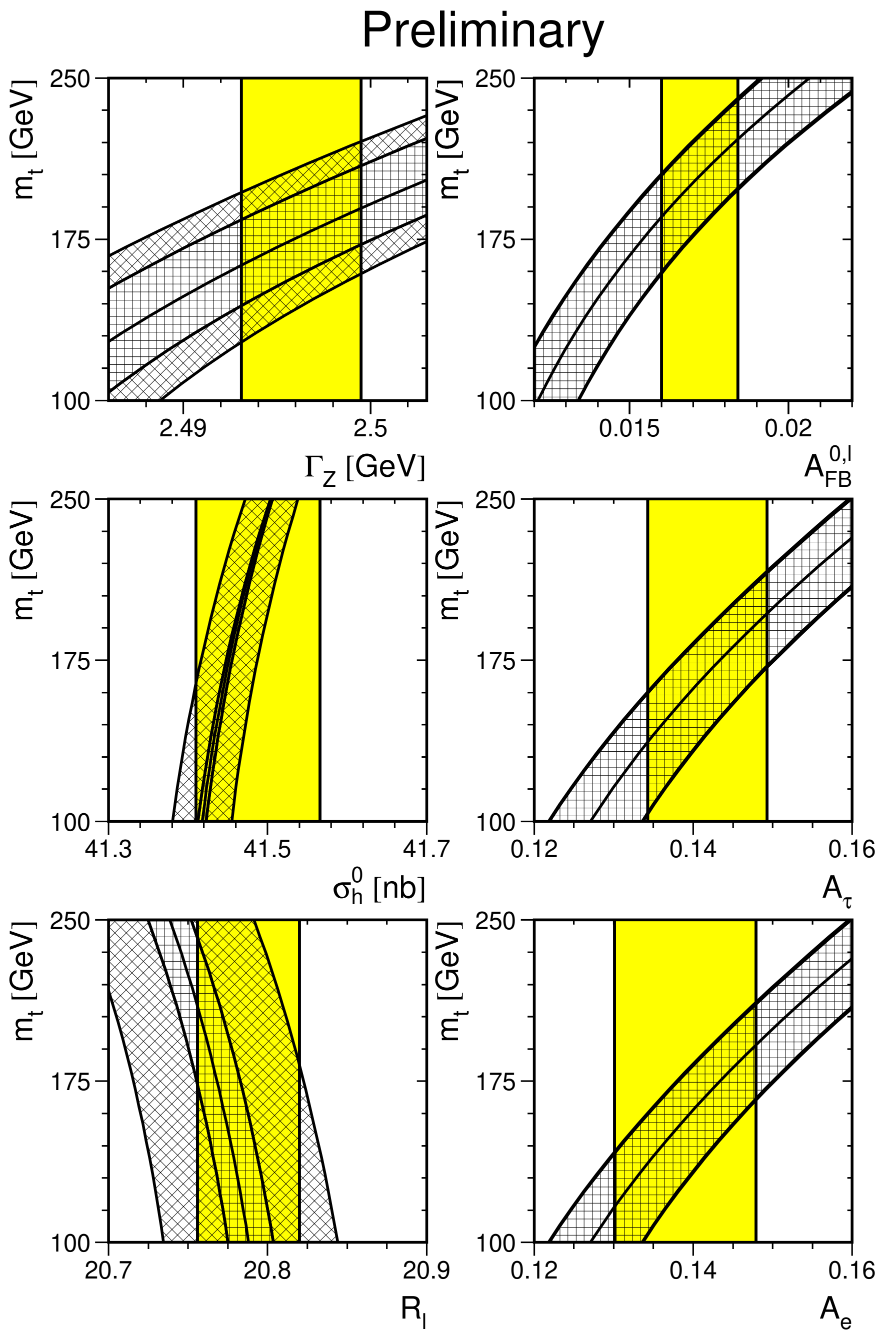

FIG. 5. Comparison of LEP measurements with Standard Model predictions as a function of M_{top}. The experimental errors on the parameters are indicated as vertical bands. The cross-hatch pattern parallel to the axes indicates the variation of the Standard Model prediction with M_{Higgs} spanning the interval $60 \leq M_{Higgs} \leq 1000\ \mathrm{GeV/c}^2$, and the diagonal cross-hatch pattern corresponds to a variation of $\alpha_s(M_Z^2)$ within the interval $\alpha_s(M_Z^2) = 0.123 \pm 0.006$. The total width of the band corresponds to the linear sum of both uncertainties (The LEP Collaborations, 1995).

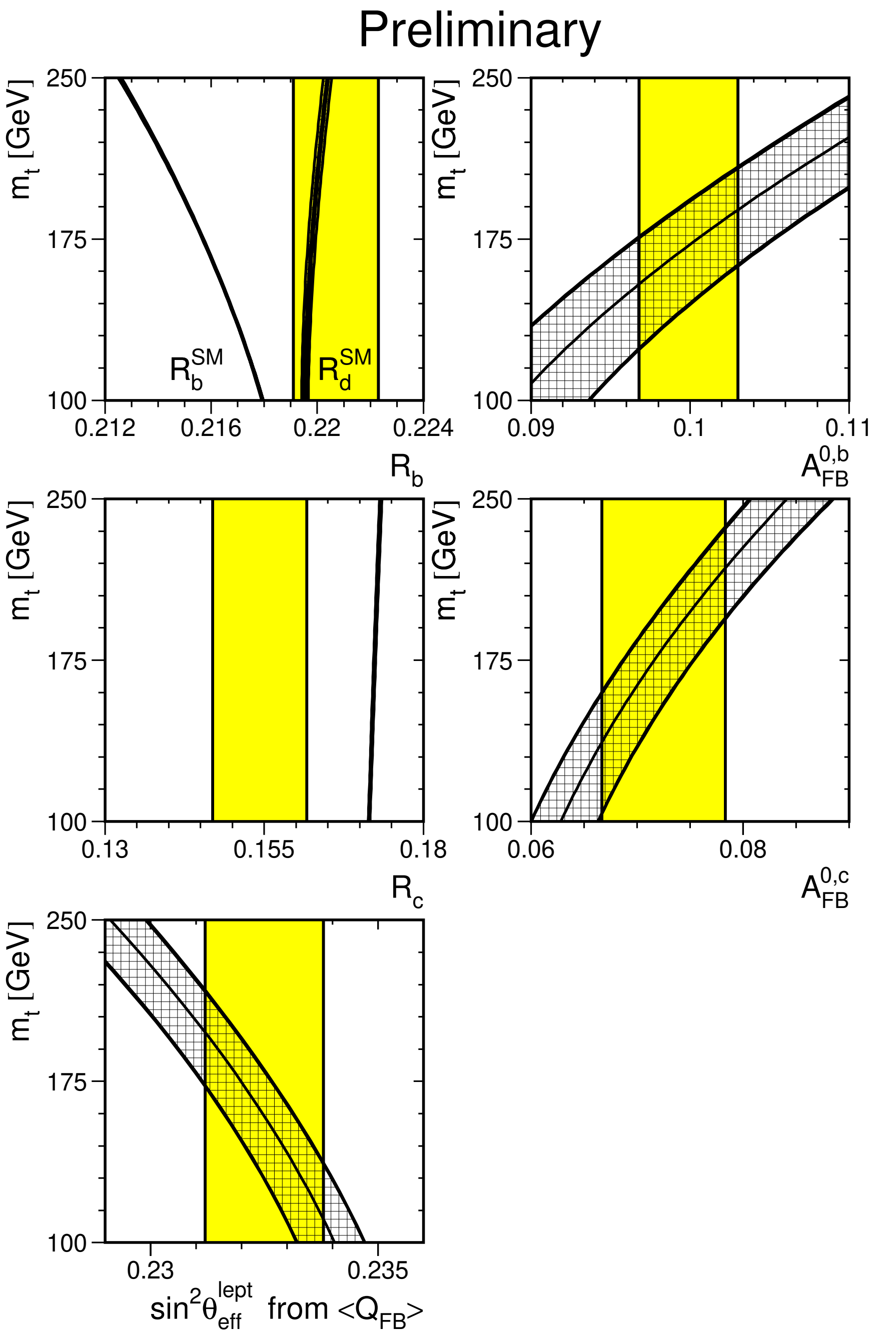

FIG. 6. Comparison of LEP measurements with Standard Model predictions as a function of M_{top} as in the previous figure. For the ratios of the partial widths the variations with M_{Higgs} and $\alpha_s(M_Z^2)$ nearly cancel. For the comparison of R_b with the Standard Model the value R_c has been fixed to its Standard Model prediction. To illustrate the impact of special vertex corrections to R_b, the Standard Model prediction for R_d is also shown (The LEP Collaborations, 1995).

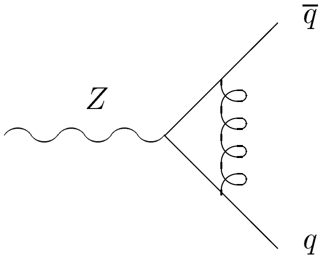

FIG. 7. One Feyman diagram illustrating a QCD correction to the Z width.

2. R$_b$

The decay of the Z into $b\overline{b}$ is of particular interest, because it is sensitive through weak vertex corrections to the top quark mass, (see Fig. 9). The dependence of all the Z partial widths on the Higgs mass is due mostly to corrections to the Z propagator. Therefore, in R$_b$, the ratio of $\Gamma_Z^{b\overline{b}}$ to $\Gamma_Z^{hadrons}$, most of the Higgs and α_s dependence cancels. This ratio then gives the only indirect measurement of the top mass independent of the Higgs mass. A comparison between the experimental measurement and the theoretical prediction is a particularly good test of the Standard Model and possibly the first place to look for new (non-Standard Model) physics.

The value of R$_b$ from the combinations of many measurements at LEP and SLC is higher than expected, whereas the value of R$_c$ is lower than expected. The measurement of R$_b$ depends on what is assumed for R$_c$ because charm quarks are a background to the bottom quark signal in the data. Because the two are correlated, R$_b$ is quoted either assuming a Standard Model value for R$_c$, or the measured value. In Fig. 10 we show the LEP measurements of R$_c$ vs. R$_b$, together with the Standard Model theoretical prediction based on the direct measurement of the top quark mass performed at the Tevatron (see Section IX). The disagreement between data and theory may be an indication of new physics beyond the Standard Model (see for example Altarelli *et al.* 1996; Wells and Kane, 1995).

B. W mass

The W vector boson mass (M$_W$) also depends on the top quark and Higgs masses through loop diagrams like those shown in Fig. 11, in which $W \to t\overline{b} \to$W, or $W \to WH \to W$. A precise measurement of M$_W$ constrains the top mass for a fixed Higgs mass. When combined with a precise measurement of the top mass, such a measurement can provide information on the Higgs mass, or, in the case of disagreement with theory, can signal the presence of new physics. Even with precise direct measurements of M$_{top}$ and M$_W$, however, the constraints on M$_{Higgs}$ are weak, because the Higgs mass dependence is only logarithmic. The present status of the W and top mass measurements, and their comparison with theory, is summarized in Fig. 12.

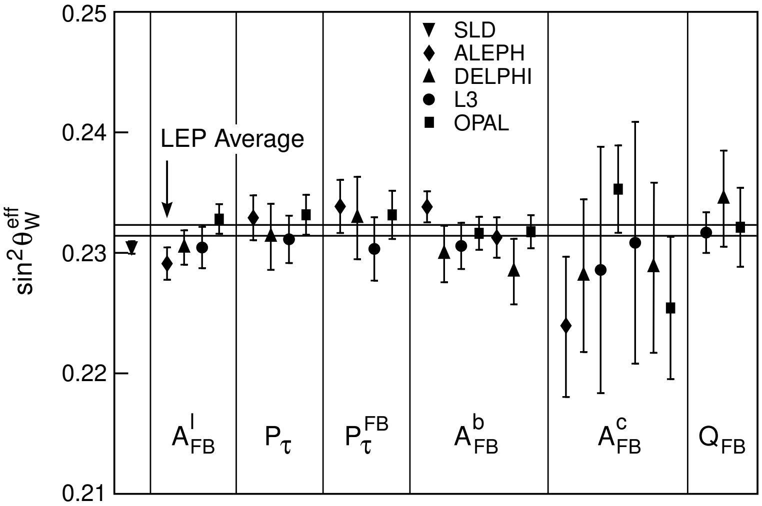

FIG. 8. A summary of the measurements of $\sin^2\theta_{eff}^{lept}$ from LEP and SLC. The leftmost point is the value from A_{LR} at SLD; $\sin^2\theta_{eff}^{lept} = 0.2305 \pm 0.0005$. The LEP average is $\sin^2\theta_{eff}^{lept} = 0.2319 \pm 0.0004$. (Woods, 1996).

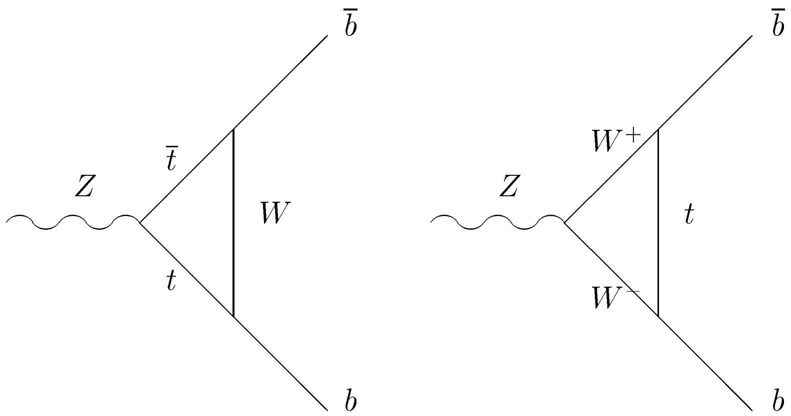

FIG. 9. Diagrams showing t-quark corrections to $Z \to b\bar{b}$.

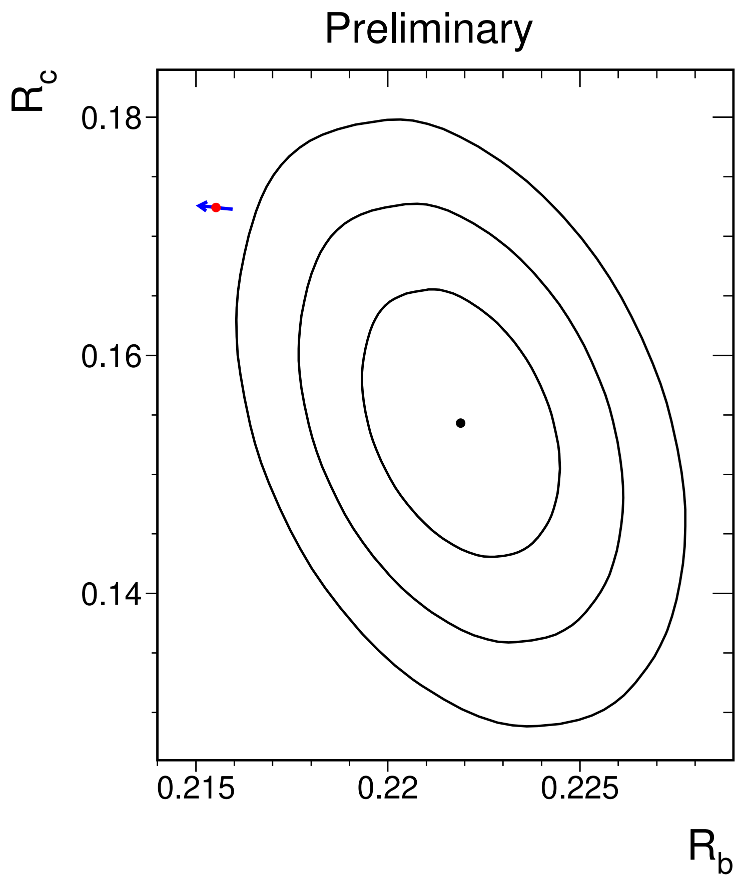

FIG. 10. Contours in the R_b - R_c plane derived from LEP data, corresponding to 68%, 95% and 99.7% confidence levels assuming Gaussian systematic errors. The Standard Model prediction for $M_{top} = 180 \pm 12$ GeV/c^2 is also shown as a dot with an arrow through it. (This is the average of the 1995 CDF and D0 top mass measurements; the current average is 175 ± 8 GeV/c^2). The arrow points in the direction of increasing values of M_{top} (The LEP Collaborations, 1995).

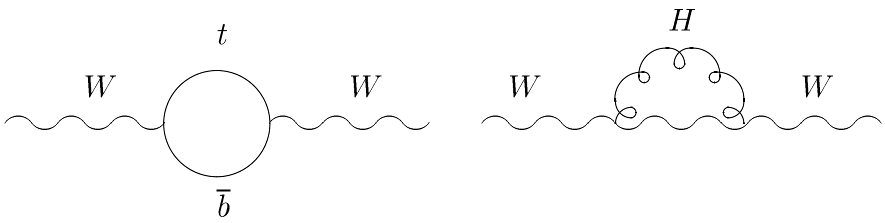

FIG. 11. Lowest order radiative corrections to the W mass involving top and bottom quarks and the Higgs.

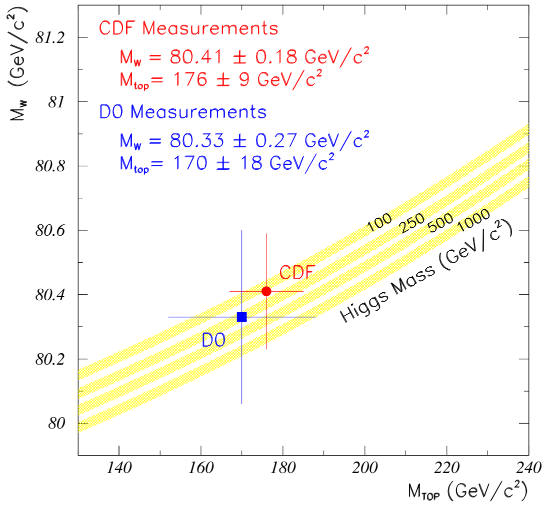

FIG. 12. W mass and top quark mass measurements from the Fermilab collider experiments (CDF and D0). The top mass values are from the full Tevatron data sets, with an integrated luminosity of $\approx$ 100 pb^{-1}. The W mass values are derived from analyses of the first 15-20 pb^{-1} only. The lines are Standard Model predictions for four different Higgs masses (Flattum,1996).

C. Global fits for M$_{top}$ and M$_{Higgs}$

Combining the indirect information from the neutral current experiments and the W mass measurement, a global fit for M$_{top}$ has been made by the LEP Electro-Weak Working Group (The LEP Collaborations, 1995). The fits are made with α_s and M$_{top}$ as free parameters, since α_s at the Z mass has a large uncertainty. The best predicted value for M$_{top}$ using data from LEP, SLC, the Fermilab collider W mass measurements and ν N scattering data, is M$_{top}$ $= 178 \pm 8^{+17}_{-20}$ GeV/c^2, with $\alpha_s = 0.123 \pm 0.004 \pm 0.002$ and with $\chi^2/d.o.f. = 28/14$ (where we have chosen M$_{Higgs}$ $= 300$ GeV/c^2 to quote the goodness of fit). The second uncertainty in this fit to the top mass comes from varying M$_{Higgs}$ from 60 GeV/c^2 to 1 TeV/c^2. The fit results are in good agreement with the directly measured values of α_s and M$_{top}$, $\alpha_s(M_Z) = 0.123 \pm 0.006$ (Bethke, 1995) and M$_{top}$ $= 175 \pm 8$ GeV/c^2, see Section IX. The variation of the fit-χ^2 as a function of M$_{top}$ for three different choices of M$_{Higgs}$ is displayed in Fig. 13.

In conclusion, all the neutral current data, as well as the W and top mass measurements are in agreement with each other, with the exception of the measurement of R$_b$. The situation is nicely summarized in Fig. 14. In this figure, the correlation between R$_l$ and R$_b$ is due to the fact that R_l depends on the total hadronic width, and hence on $\Gamma(Z \to b\bar{b})$. Given the measured value of R_l and α_s, and assuming Standard Model dependence of the partial widths on $\sin^2\theta_{eff}^{lept}$ for all but the b-quarks, R_l constrains R_b and $\sin^2\theta_{eff}^{lept}$. These three measurements are compared with the Standard Model prediction given the measured top mass. The measured values of R_b and R_c are somewhat inconsistent with the combination of $\sin^2\theta_{eff}^{lept}$, R_l and M_{top} within the context of the Standard Model.

Despite the large number of very precise measurements, there is still little information on the mass of the Higgs boson, although the data seems to prefer a low value for M_{Higgs}, (see Fig. 13). An estimate for the Higgs mass can be made using all the neutral current and hadron collider data as shown in Fig. 15. The best estimate of the Higgs mass is shown with and without the R_b and R_c measurements included. In all cases a Higgs mass less than 300 GeV/c^2 is favored with large uncertainty.

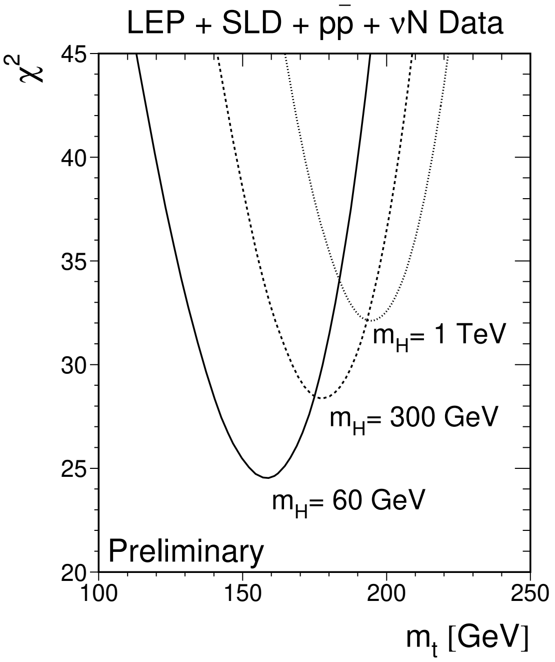

FIG. 13. The χ^2 curves for the Standard Model fit to the electro-weak precision measurements from LEP, SLD, CDF and D0 (W mass only) and neutrino scattering experiments as a function of M_{top} for three different Higgs mass values spanning the interval 60 GeV/c^2 $\leq M_{Higgs} \leq$ 1000 GeV/c^2. The number of degrees of freedom is 14 (The LEP Collaborations, 1995).

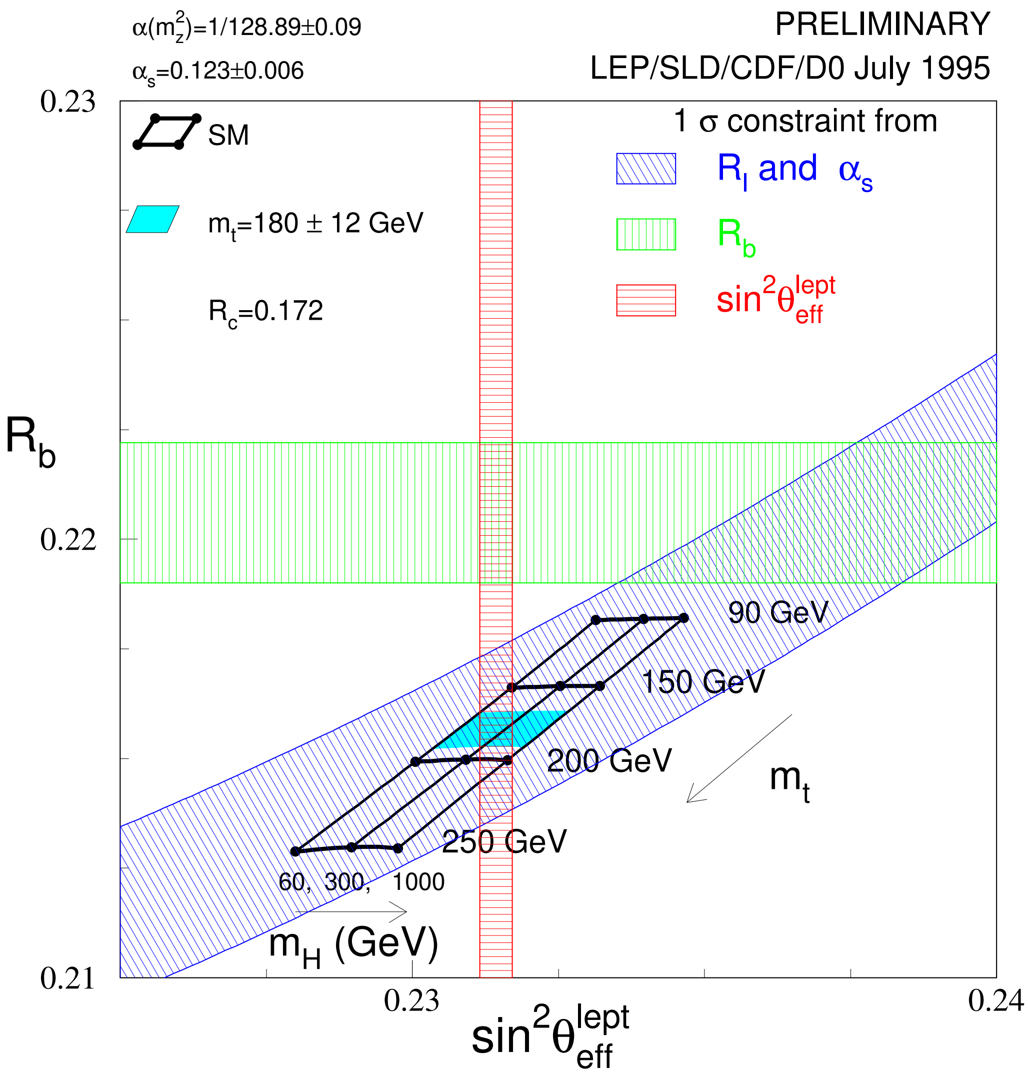

FIG. 14. The combined LEP/SLD measurements of $\sin^2\theta_{eff}^{lept}$ and R_b assuming the Standard Model value of $R_c = 0.172$ and the Standard Model prediction. Also shown is the constraint resulting from the measurement of R_l on these variables, assuming $\alpha_s(M_Z^2) = 0.123 \pm 0.006$, as well as the Standard Model dependence of light-quark partial widths on $\sin^2\theta_{eff}^{lept}$ (The LEP Collaborations, 1995).

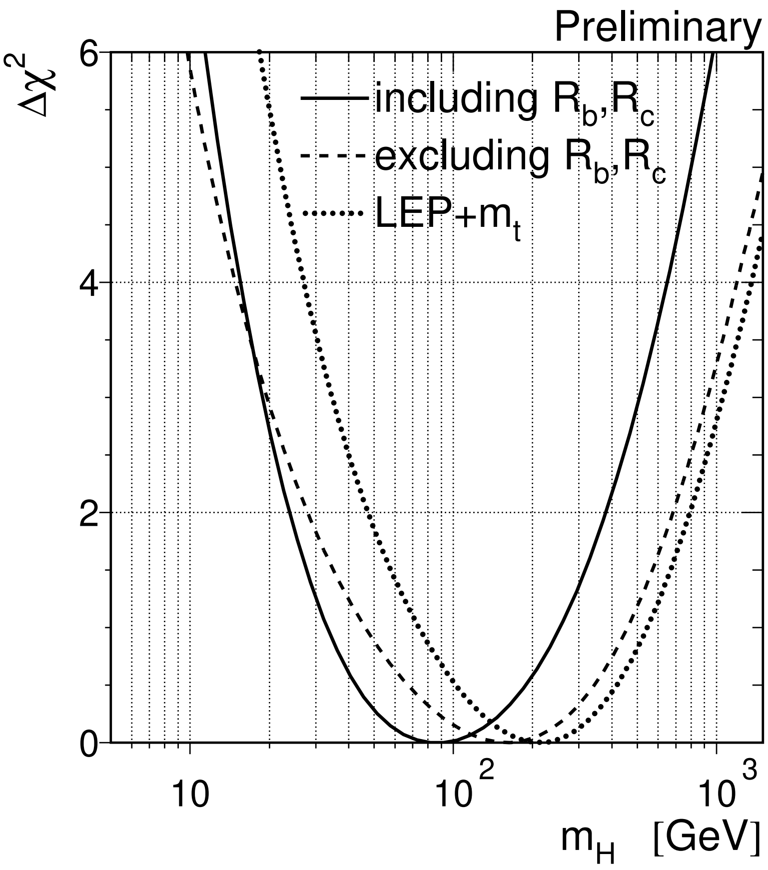

FIG. 15. $\Delta\chi^2 = \chi^2 - \chi^2_{min}$ vs M_{Higgs} curves. The continuous line uses all the data from neutral currents and $p\overline{p}$. The dashed line excludes the LEP and SLD R_b and R_c measurements. The dotted line excludes the SLD data (The LEP Collaborations, 1995).

IV. TOP QUARK PRODUCTION

Because of its large mass, the top quark can only be observed directly in collider experiments, where sufficiently high center-of-mass energies ($\sqrt{s}$) have been achieved. In electron-positron collisions, top quarks are produced in pairs via a photon or a Z. Since at lowest order this is a purely electro-weak process, the cross section and production kinematics can be precisely predicted. Today's highest energies e^+e^- accelerators, LEP at CERN and SLC at SLAC, operate at $\sqrt{s} \approx \mathrm{M}_z \approx 91$ GeV, and therefore the mass region $\mathrm{M}_{top} > 46$ GeV/c^2 cannot be explored. Searches for top in e^+e^- collisions will be briefly reviewed in Section VI. The HERA electron-proton collider at DESY has achieved a center-of-mass energy of ≈ 310 GeV. However the top production cross section at HERA is too small for observation and study of the top quark.

Significantly higher center-of-mass energies have been achieved at hadron colliders. The $p\bar{p}$ collider at CERN (the S$p\bar{p}S$), which operated between 1981 and 1989, reached $\sqrt{s} =$ 630 GeV; the $p\bar{p}$ collider at Fermilab (the Tevatron) came on line in 1987 with $\sqrt{s} = 1800$ GeV = 1.8 TeV; a new pp collider (LHC, $\sqrt{s} = 14$ TeV) is under development at CERN, and is expected to begin operation in 2003. Until a very high energy e^+e^- machine is built, top quark physics can be directly pursued only at hadron colliders. In this Section we will concentrate on the production of top quarks in $p\bar{p}$ collisions. Top quarks are produced by colliding partons (quarks, gluons, and antiquarks) from the proton and anti-proton. Therefore many aspects of our discussion also apply to other (e.g. pp) hadron-hadron collisions. Because the partons carry only a fraction of the momentum of the hadron, the center-of-mass energies of parton-parton collisions span a wide range of energies, see the discussion of parton luminosities in Section IV.A.

A. Production mechanisms and cross sections

There are three mechanisms for top production in $p\bar{p}$ collisions :

- Pair production of top quarks, $p\bar{p} \to t\bar{t}$ + X. The leading order Feynman diagrams for this process are shown in Fig. 16. At higher order, gluon-quark scattering also contributes. $t\bar{t}$ pairs can also be produced through a Z or a photon, however the cross section is much smaller and we will not consider this possibility further.

- Drell-Yan production of a W boson, with subsequent decay into $t\bar{b}$, i.e. $p\bar{p} \to$W + X; $W \to t\bar{b}$, (see Fig. 17). Except for small contributions from off mass-shell W boson production, this mechanism only contributes for top masses smaller than $\mathrm{M}_W - \mathrm{M}_b$.

- Single top-quark production via W-gluon fusion, see Fig 18. Photon-gluon and Z-gluon fusion are also allowed, with a much lower cross section.

As will be illustrated in this Section, at Fermilab's Tevatron the strong-interaction pair production process ($p\bar{p} \to t\bar{t}$) is dominant over a wide range of top masses. For $\mathrm{M}_{top} \approx 60$ GeV/c^2, the top production rate from $W \to t\bar{b}$ is comparable to that of $t\bar{t}$. For very high top mass, above $\mathrm{M}_{top} \approx 220$ GeV/c^2, the expected cross section for single top production

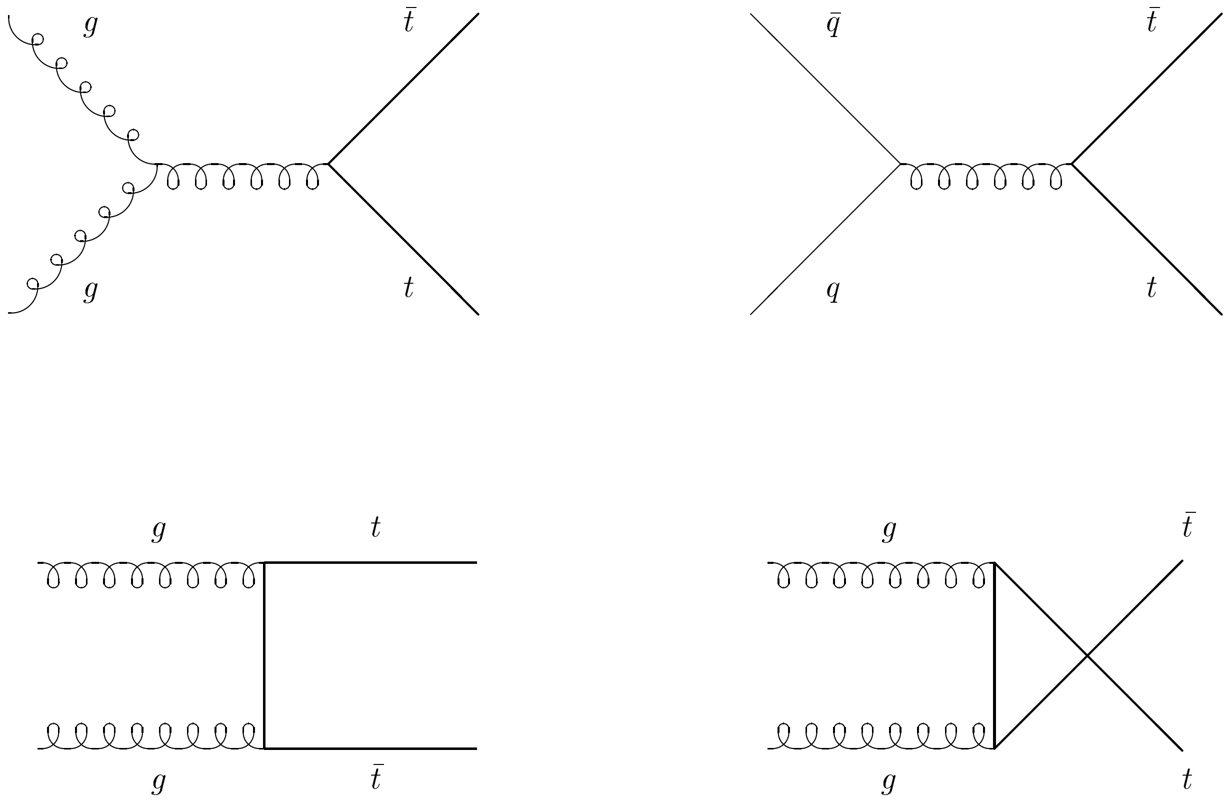

FIG. 16. Lowest order Feynman diagrams for production of $t\bar{t}$ pairs in $p\bar{p}$ collisions.

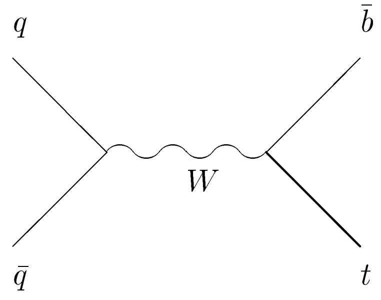

FIG. 17. Lowest order Feynman diagram for Drell-Yan production of $t\bar{b}$ pairs, $p\bar{p} \to W \to t\bar{b}$.

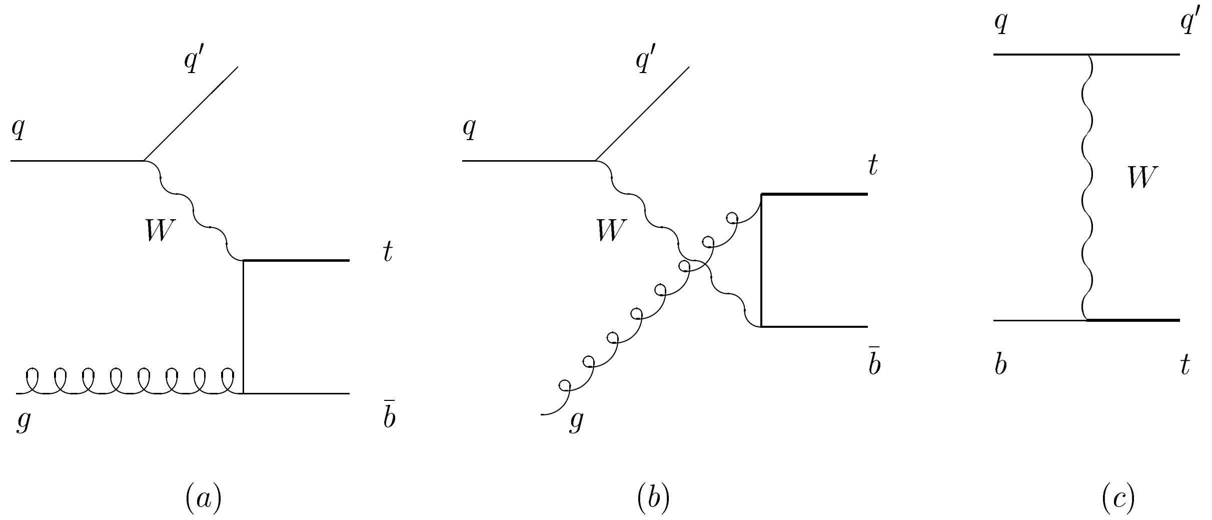

FIG. 18. Lowest order Feynman diagrams for production of a single top quark via W-gluon fusion in $p\bar{p}$ collisions. When combining diagrams (a) and (c), care must be exercised to avoid double counting and to define the b-quark distribution inside the proton in a consistent fashion (Heinson, Belyaev, and Boos, 1995; Carlson and Yuan, 1995).

through W-gluon fusion becomes larger than the pair production cross section due to the very high parton center-of-mass energy required to produce a $t\bar{t}$ pair (see discussion below).

The pair production cross section for heavy quarks such as the top can be calculated in perturbative QCD. It factorizes as a product of the parton distribution functions inside the protons and the parton-parton point cross section, and is written as a sum over contributions from partons inside the proton and anti-proton (Collins, Soper, and Sterman, 1986) :

$$\sigma(p\bar{p} \to t\bar{t}) = \sum_{i,j} \int dx_i F_i(x_i, \mu^2) \int dx_j F_j(x_j, \mu^2) \hat{\sigma}_{ij}(\hat{s}, \mu^2, M_{top}).$$

The functions F_i and F_j are the number densities of light partons (quarks, antiquarks, and gluons) evaluated at a scale μ in the proton and anti-proton; x_i and x_j are the momentum fractions of the incoming partons, i.e. parton i (j) has momentum x_iP $(-x_jP)$, where P is the magnitude of the proton momentum in the center of mass frame (which in colliding beam experiments coincides with the lab frame); $\hat{\sigma}_{ij}$ is the point cross section for $i + j \to t\bar{t}$ and $\hat{s} = 4x_ix_jP^2 = x_ix_js$ is the square of the center of mass energy of the parton-parton collision. The factorization and renormalization scale μ is an arbitrary parameter with dimensions of energy, which is introduced in the renormalization procedure. The exact result for the cross section should be independent of the value of μ. However, since calculations are performed to finite order in perturbative QCD, cross-section predictions are in general dependent on the choice of scale, which is usually taken to be of the order of M$_{top}$. The sensitivity of perturbative calculations to reasonable variations in μ is used to estimate the accuracy of the prediction. Parametrizations of the parton number densities (F_i and F_j) are extracted from fits to a large number of experimental results, mostly from deep inelastic scattering, see for example Fig. 19.

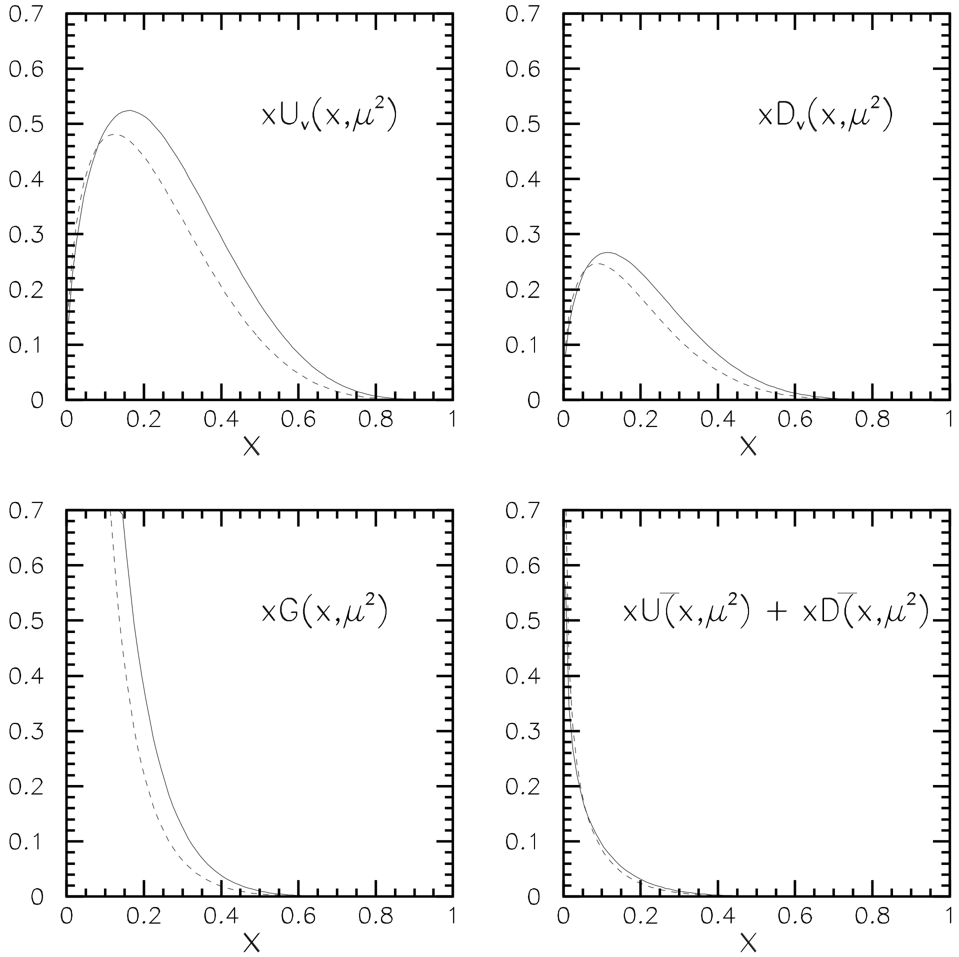

FIG. 19. MT-B2 parametrization (Morfin and Tung, 1991) of xF_i for valence u-quarks, $xU_v(x,\mu^2)$, valence d-quarks, $xD_v(x,\mu^2)$, gluons, $xG(x,\mu^2)$, and sea u- and d-quarks, $x\bar{U}(x,\mu^2)+x\bar{D}(x,\mu^2)$. These are calculated at $\mu^2 = (20\ \mathrm{GeV})^2$ (solid line) and $\mu^2 = (400\ \mathrm{GeV})^2$ (dashed line). The $t\bar{t}$ cross section is usually calculated with $\mu^2 = \mathrm{M}_{top}^2$.

The cross section for $p\bar{p} \to t\bar{t}$ can also be written as (Eichten *et al.*, 1984) :

$$\frac{d\sigma}{d\tau} = \sum_{ij} \frac{dL_{ij}}{d\tau} \hat{\sigma}_{ij}(\hat{s}, \mu^2, M_{top})$$

where $\tau = \hat{s}/s$ and $dL_{ij}/d\tau$ are the differential parton luminosities defined as :

$$\frac{dL_{ij}}{d\tau} = \frac{1}{1+\delta_{ij}} \int_{\tau}^{1} \frac{dx}{x} \left[F_i(x,\mu^2)F_j(\tau/x,\mu^2) + F_j(x,\mu^2)F_i(\tau/x,\mu^2)\right].$$

The parton luminosities for quark-antiquark and gluon-gluon processes at Tevatron energies are displayed in Fig. 20. The sharp fall-off of these luminosities with increasing $\hat{s}$, as well as the asymptotic $1/\hat{s}$ dependence of $\hat{\sigma}$, result in predictions for the $t\bar{t}$ cross-sections which fall steeply as a function of M_{top}. At $\sqrt{s} = 1.8$ TeV the gg luminosity is larger than the $q\bar{q}$ luminosity up to $\hat{s} \approx (220\ \mathrm{GeV})^2$. As a result, top pair production is dominated by the $gg \to t\bar{t}$ process up to $M_{top} \approx 90$ GeV/c^2. For higher top quark mass, $q\bar{q}$ initial states are the most important source of $t\bar{t}$ pairs.

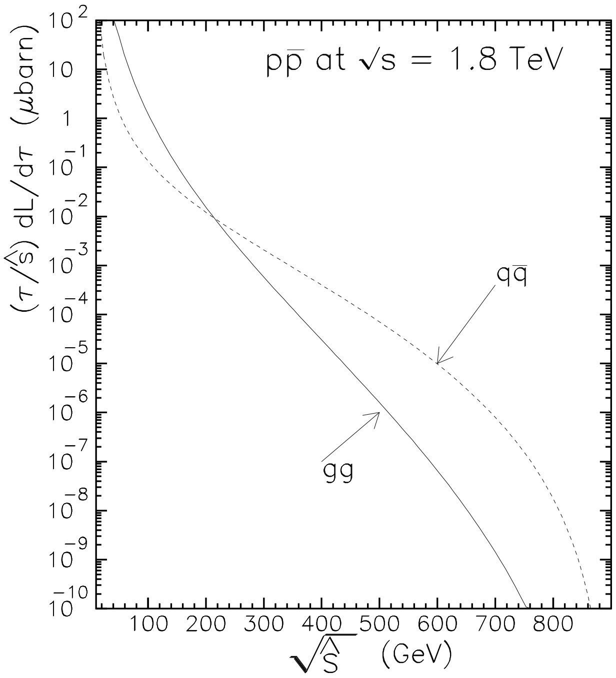

FIG. 20. Gluon-gluon (gg) and quark-antiquark ($q\bar{q} = u\bar{u} + d\bar{d} + s\bar{s}$) parton luminosities in $p\bar{p}$ collisions at $\sqrt{s} = 1.8$ TeV. These are calculated using the MT-B2 parametrization of the parton distribution functions (Morfin and Tung, 1991) evaluated at a scale $\mu^2 = \hat{s}$.

The leading order (LO) cross section for producing a pair of heavy quarks in parton-parton collisions was calculated in the late 1970's (Gluck, Owens, and Reya, 1978; Combridge, 1979; Babcock, Sivers, and Wolfram, 1978; Hagiwara and Yoshino, 1979; Jones and Wyld, 1978; Georgi *et al.*, 1978). The full next-to-leading order (NLO) calculation was performed by Nason, Dawson, and Ellis in 1988, and shortly afterwards by Beenaker *et al.*, 1991. On the basis of their result, cross-section predictions were then made (Altarelli *et al.*, 1988; Ellis, 1991) by convoluting the partonic cross-section with parametrizations of the parton distribution functions.

There are two sources of uncertainty in such a calculation of the $p\bar{p} \to t\bar{t}$ cross-section as a function of M_{top}. As mentioned above, the first uncertainty is due to the nature of the perturbative QCD calculation for the partonic cross-section ($\hat{\sigma}$). The size of the uncertainty is customarily quantified by varying the arbitrary value of the scale μ by a factor of two around the top mass. Note that this is not a rigorous procedure, and it merely results in a *reasonable* estimate of the systematic uncertainty due to the missing higher order terms in the calculation. An additional uncertainty arises from the limited knowledge of the input parton distribution functions, and the assumed value of the QCD parameter Λ_{QCD}. The Λ_{QCD}-dependence arises from the fact that the assumed value of Λ_{QCD} affects the μ^2 evolution of both α_s and the quark and gluon distributions. In particular, the extraction of the gluon distribution from deep inelastic data also depends on Λ_{QCD}. The uncertainty on the cross-section calculation due to the parton distribution uncertainties are

Calculation	Order	$\sigma(t\bar{t})$
(1) Ellis, 1991	NLO	$4.20^{+0.28}_{-0.54}$ pb
(2) Laenen, Smith and van Neerven, 1994	NLO + gluon resummation	$4.94^{+0.71}_{-0.45}$ pb
(3) Berger and Contopanagos, 1995	NLO + gluon resummation	$5.52^{+0.07}_{-0.45}$ pb
(4) Catani *et al.*, 1996	NLO + gluon resummation	$4.75^{+0.63}_{-0.68}$ pb

TABLE II. Calculations of the $p\bar{p} \to t\bar{t}$ cross-sections at Tevatron energies for $M_{top} = 175$ GeV/c^2. Note that these cross-section calculations use different sets of parton distribution functions (PDFs). The systematic uncertainties in (2) and (3) do not include the effects of varying the input PDFs.

very hard to quantify. This uncertainty is usually estimated by studying the variations of the calculated cross-section using different parametrizations for the parton distribution functions and different values of Λ_{QCD}. As a result of these studies, the total theoretical uncertainty on the $t\bar{t}$ production cross-section at $\sqrt{s} = 1.8$ TeV is estimated to be of order $\pm$ 20%. The uncertainties due to the choice of scale and to the parton distribution assumptions are found to contribute approximately the same amount to the total uncertainty.

The next-to-leading-order, $O(\alpha_s^3)$, predictions for the pair production cross-section have been subsequently refined by Laenen, Smith, and van Neerven (1992 and 1994). In their calculation the corrections due to initial state gluon brehmstrahlung, which are large near $t\bar{t}$ threshold, have been resummed to all orders in perturbative QCD, and have been included in the computation. This procedure introduces a new scale $\mu_0 >> \Lambda_{QCD}$, where the resummation is terminated since the calculation diverges as $\mu_0 \to 0$, where nonperturbative effects are expected to dominate. Given that the corrections due to soft gluons have been shown to be positive at all orders in perturbative QCD for $\mu = M_{top}$, they estimate the lower limit on the $t\bar{t}$ cross-section as the sum of the full $O(\alpha_s^3)$ prediction and the $O(\alpha_s^4)$ soft gluon correction, using the conservative value of $\Lambda_{QCD} = 105$ MeV. Their best estimate of the cross section includes the full gluon resummation contributions, and the uncertainty arises mostly from the choice of μ_0, which is allowed to become as small as $0.05M_{top}$ and $0.2M_{top}$ for the $q\bar{q} \to t\bar{t}$ and $gg \to t\bar{t}$ channels respectively.

A separate calculation of the $t\bar{t}$ cross-section including the perturbative resummation of gluon radiative corrections has become available in the past year (Berger and Contopanagos, 1995). This calculation is based on Principal Value Resummation (PVR) techniques (Contopanagos and Sterman, 1993 and 1994), and is independent of the arbitrary infrared cutoff μ_0. Theoretical uncertainties are estimated by varying the renormalization and factorization scale μ by a factor of two around the top mass. A more recent evaluation of the effects of gluon resummation suggests that its contribution is much smaller than previously thought (Catani *et al.*, 1996). In Table II we summarize the results of the various calculations of the $p\bar{p} \to t\bar{t}$ cross-section at Tevatron energies for a top mass of 175 GeV/c^2 which, as we will discuss in Section IX, corresponds to the directly measured value of the top mass.

The expected top production cross-sections at Tevatron and S$p\bar{p}$S energies, for the three production mechanisms, are displayed in Fig. 21 and Fig. 22. The Drell-Yan cross section, $\sigma(p\bar{p} \to W \to t\bar{b})$, is calculated from the diagram shown in Fig. 17. The value of this cross

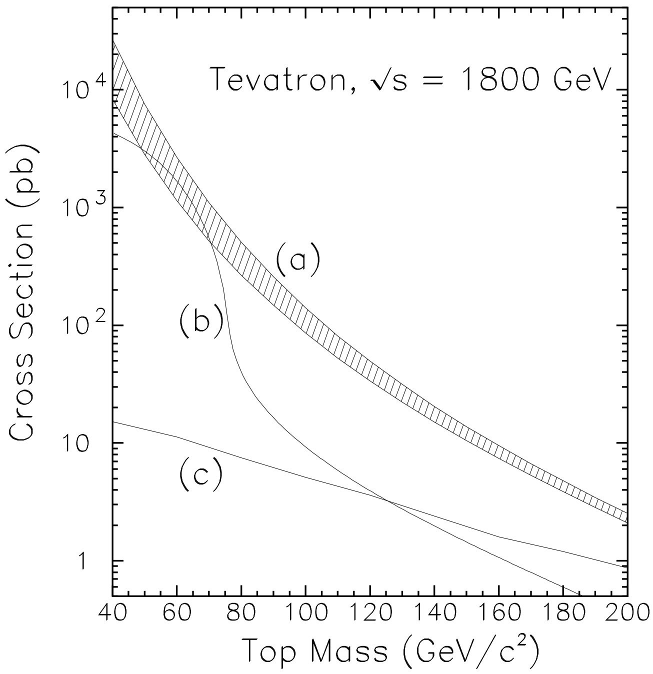

FIG. 21. Top production cross-sections in $p\bar{p}$ collisions at $\sqrt{s} = 1.8$ TeV. (a) $p\bar{p} \to t\bar{t}$ from Laenen, Smith and van Neerveen, 1994. The band represents the estimated theoretical uncertainty; (b) sum of $t\bar{b}$ and $\bar{t}b$ from W decay (Drell-Yan); (c) sum of $t\bar{b}$ and $\bar{t}b$ from W-gluon fusion. See text for details.

section is normalized to the rate of W production through measurements of $p\bar{p} \to W \to e\nu$ (F. Abe *et al.*, 1991b; Alitti, *et al.*, 1990a; Albajar *et al.*, 1991a), including corrections for the phase-space suppression of a $t\bar{b}$ pair and the finite W width. The tree-level W-gluon fusion cross-section has been calculated by several authors (Willenbrock and Dicus, 1986; Yuan, 1990; Anselmo, van Eijk, and Bordes, 1992; Ellis and Parke, 1992; Bordes and van Eijk, 1993); the cross sections shown in Figs. 21 and 22 are obtained using the PYTHIA Monte Carlo event generator (Sjöstrand and Bengtsson, 1987). Since the W-gluon fusion matrix element is calculated at tree level, the systematic uncertainties on the absolute rate prediction can be large, see for example Ellis and Parke, 1992. Here we have used the default PYTHIA scale $\mu^2 = 0.5$ ($\mathrm{M}_{t1}^2 + \mathrm{M}_{t2}^2$), where M_{t1} and M_{t2} are the transverse masses of the outgoing partons. Recently, a calculation of the next-to-leading order QCD corrections for the W-gluon fusion process has been performed (Bordes and van Eijk, 1995), and the enhancement of the cross section over the Born-level result has been found to be of order 30%. It is worth mentioning that, despite their apparent similarities, the Drell Yan and W-gluon mechanisms are quite distinct. The higher order Drell-Yan diagram, $qg \to qW^*$, $W^* \to t\bar{b}$ (see Fig. 23) and the W-gluon fusion diagrams (see Fig. 18) have the same initial and final state partons. However, in one case the W is space-like, and in the other case it is time-like. Furthermore, the $t\bar{b}$ pairs in the two processes are in different color states.

As anticipated, the pair production cross-section at the Tevatron (see Fig. 21) is dominant up to very high mass, except for the top mass region around 60 GeV/c^2, where the cross sections for the $t\bar{t}$ and $W \to t\bar{b}$ processes are approximately equal. On the other hand, at

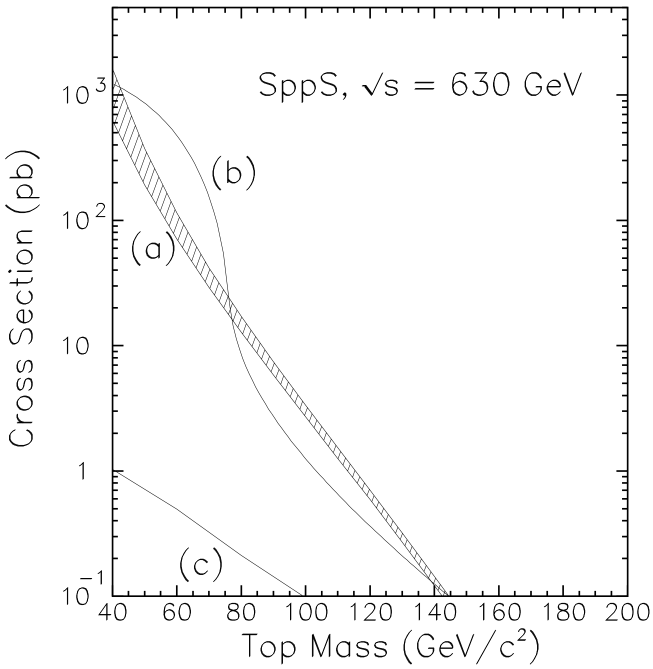

FIG. 22. Top production cross-sections in $p\bar{p}$ collisions at $\sqrt{s} = 0.63$ TeV. (a) $p\bar{p} \rightarrow t\bar{t}$ from Laenen, Smith and van Neerveen, 1994. The band represents the estimated theoretical uncertainty; (b) sum of $t\bar{b}$ and $\bar{t}b$ from W decay (Drell-Yan); (c) sum of $t\bar{b}$ and $\bar{t}b$ from W-gluon fusion. See text for details.

the lower energy of the S$\bar{p}p$S collider, top production through W decay dominates in the mass region 40-80 GeV/c^2, (see Fig. 22). Once the experimental evidence started pointing towards higher top masses (see Section VI), it became clear that top searches at the S$\bar{p}p$S were not competitive with those at the Tevatron, due to the lower $t\bar{t}$ cross-section at $\sqrt{s} =$ 630 GeV.

It should be emphasized that top production is a very rare process in $p\bar{p}$ collisions. The total inelastic cross-section at the Tevatron is approximately 60 mb (F. Abe *et al.*, 1994b), ten orders of magnitude higher than $\sigma(t\bar{t})$ for $M_{top} = 175$ GeV/c^2. Therefore, in trying to isolate a top signal, both excellent background rejection and high luminosities are critical.

In the remainder of this Section and in most of this review we will concentrate on the $p\bar{p} \rightarrow t\bar{t}$ reaction. We will however revisit the W-gluon fusion process in Section X, since it is interesting in its own right and its study will become accessible in the not too distant future.

B. Top quark hadronization

Quarks are not observed as free particles but are confined to form hadronic bound states. The top quark however is unique in that its mass is high enough that it can decay before hadronization. According to the Standard Model, top quarks undergo the weak decay $t \rightarrow Wb$, where the W boson is real if $M_{top} > M_W + M_b$, and virtual otherwise. Decay modes such as $t \rightarrow Ws$ and $t \rightarrow Wd$ are also allowed. They are suppressed by factors of $|V_{ts}|^2/|V_{tb}|^2 \approx$

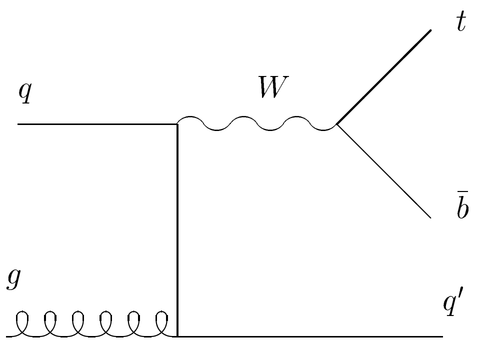

FIG. 23. Diagram contributing to the O(α_s) corrections to the Drell-Yan process $p\bar{p} \to W \to t\bar{b}$.

10^{-3} and $|V_{td}|^2/|V_{tb}|^2 \approx 5$ x 10^{-4} respectively, where V_{ij} is a Cabibbo-Kobayashi-Maskawa (CKM) mixing-matrix element (Montanet *et al.*, 1994). The expected width of the top quark, and hence the lifetime, as a function of its mass, is shown in Fig. 24.

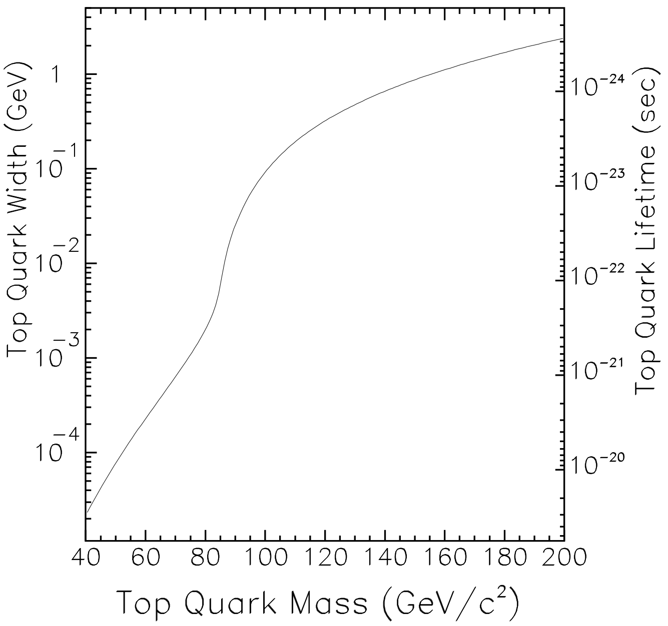

FIG. 24. The Standard Model width of the top quark as a function of its mass (Bigi, 1986). Note the transition between the region of virtual and real W decays which occurs at $M_{top} \approx M_W + M_b$.

The hadronization process, which is non-perturbative in nature, is not well understood. However, the formation of hadrons is estimated to take place in a time of order $\Lambda_{QCD}^{-1} \approx$ O(100 MeV)$^{-1} \approx$ O(10^{-23}) seconds (Bigi, 1986). As can be seen in Fig. 24, the top lifetime becomes shorter than this characteristic time if the top mass is higher than approximately 100 GeV/c^2. A more quantitative treatment is given by Orr (1991), and is briefly summarized here. In this model, the t and the $\bar{t}$ emerging from the hard scatter are linked by color strings to the remnants of the proton and anti-proton. When the separation between the outgoing quarks and the color-connected remnants exceeds a distance of order 1 fm, the stretched color string is expected to break, resulting in the creation of fragmentation particles from the vacuum, and possibly the formation of a bound state top hadron. For $M_{top} > 165$ GeV/c^2, the top production kinematics at the Tevatron are such that essentially all top quarks are expected to decay before having travelled that minimum distance. Conversely, for top masses below 120 GeV/c^2, the overwhelming majority of top quarks will survive to a distance of 1 fm, and hadronization effects are expected to occur. Varying the assumption on the hadronization distance by a factor of two results in a mass-shift of order 20 GeV/c^2 for the transition region between hadronization and free-quark decay.

The exceedingly short top-quark lifetime is due not only to the very high mass, but also to the fact that $M_{top} > M_b$, so that the the top can decay into Wb, and this decay mode is not CKM suppressed. A heavy $I_3 = -1/2$ fourth generation quark (b') would decay into Wu', where u' here stands for an $I_3 = +1/2$ up-type quark. The decay rate would be proportional to the square of the CKM mixing-matrix element that connects b' and u'. If the b' were lighter than the fourth-generation up-type quark, then only generation-changing, CKM suppressed, decays would be allowed. As a result, the lifetime of such a fourth generation quark could be considerably longer than that of a top-quark of the same mass. Fourth generation heavy hadrons, as well as new quarkonia states, could then still be allowed to form.

Even if hadronization effects do occur in $t\bar{t}$ production, their effects, although potentially interesting, are not expected to be experimentally observable, at least in the forseeable future. The reason is that the fragmentation of heavy quarks is *hard*, i.e. the fractional energy loss of the top quark as it hadronizes is small (Peterson *et al.*, 1983). Distortions to the kinematics of the top quark from the perturbative partonic calculation are minimal. Additional particles produced in the hadronization process have little effect on the overall event topology. If a top hadron is indeed produced, the kinematics of the top decay will not be very different from that of a free quark decay since the companion quark is so much lighter. The fragmentation of the b-quark produced in top decay could potentially be more seriously affected. This is because the color string would link the b-quark to the light quark produced in the top fragmentation rather than the proton or anti-proton remnant (Orr, 1991). However, all top-quark experimental studies to date have not been precise enough to be sensitive to fragmentation assumptions.

C. Underlying event

After the hard collision, the remnants of the proton and anti-proton also hadronize. This process cannot be described within the framework of perturbative QCD, and is therefore poorly understood. The particles from the remnant hadronization form what is usually referred to as the *underlying event*. The structure of the underlying event is similar to that of the bulk of soft $p\bar{p}$ collisions (the so-called minimum bias events).

Minimum bias events are events collected with a simple interaction trigger. This trigger usually consists of a coincidence between large banks of scintillator counters in the very forward and backward regions, and is highly efficient for all types of inelastic $p\bar{p}$ collisions, except for singly diffractive events. In minimum bias events, the average transverse momentum of the hadrons is $P_T \approx 500$ MeV/c (Para, 1988). (Transverse momentum is the component of momentum perpendicular to the direction of the beams). Most of the energy is carried away by particles which remain inside the beam pipe and are not seen in the

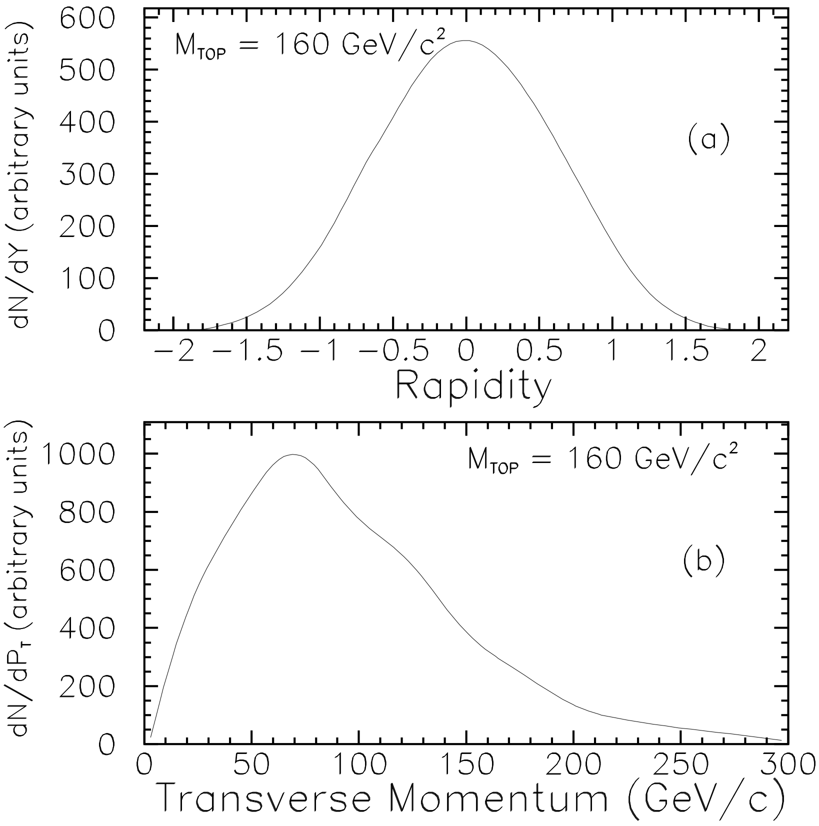

FIG. 25. The expected rapidity (y) and transverse momentum (P_T) distributions for top quarks at the Tevatron. The predictions are form the ISAJET Monte Carlo program.

detector. The charged particle multiplicity in the central region per unit pseudo-rapidity ($dN^{ch}/d\eta$) grows approximately logarithmically with the center-of-mass energy, and at $\sqrt{s} =$ 1.8 TeV is $dN^{ch}/d\eta \approx 4$ (F. Abe *et al.*, 1990e). (NB: the rapidity y of a particle is defined in terms of the longitudinal Lorentz boost, with $\beta = \tanh y$, to the frame in which the particle's momentum is purely transverse. Rapidity can be written as

$$y \;= \frac{1}{2}\,\ln \frac{E+P_z}{E-P_z} \;=\; \frac{1}{2}\,\ln \frac{(E+P_z)^2}{M^2+P_T^2}$$

where E is the energy of the particle, M is its mass, and P_z and P_T are the components of momenta parallel and transverse to the beam direction. Pseudo-rapidity (η) is the rapidity calculated neglecting the particle's mass, $\eta = -\ln \tan(\theta/2)$, where θ is the polar angle with respect to the proton direction. Zero rapidity or pseudorapidity corresponds to particles moving at 90^o from the beamline; high values of $|y|$ or $|\eta|$ implies very forward or backward going particles).

D. Modelling of top quark production

The reliability of the modeling of $t\bar{t}$ production in is an important issue. Top production is usually modelled using a QCD shower Monte Carlo program, such as ISAJET (Paige and Protopopescu, 1986), HERWIG (Marchesini and Webber, 1984 and 1988) or PYTHIA (Sjöstrand and Bengtsson, 1987). These Monte Carlos are used by the experimental groups to calculate the $t\bar{t}$ acceptance and kinematics, and to model the resolution of the top quark mass measurement, see Section IX.

In all these Monte Carlo programs, the initial hard scatter is generated from tree-level matrix elements convoluted with parametrizations of the parton distribution functions. Initial and final state partons are then developed into a gluon and $q\bar{q}$ radiation cascade, with angular and energy spectra based on the QCD Altarelli-Parisi splitting function. The QCD shower is terminated when the virtual invariant mass of the parton in the cascade becomes smaller than a minimum value which is of order 1 GeV for HERWIG and PYTHIA and 6 GeV for ISAJET, at which point perturbative QCD is expected to break down. Phenomenological models are then employed to combine the remaining partons into hadrons. The underlying event is also modelled in a phenomenological way, with a number of parameters tuned to reproduce the hadron multiplicities and transverse momentum spectra measured in soft $p\bar{p}$ collisions (minimum bias events). Short lived particles are made to decay, with branching ratios and decay models based on the compilation from the Particle Data Group (Montanet *et al.*, 1994).

The main differences between these Monte Carlo event generators reside in the modeling of the radiation processes. ISAJET employs an independent fragmentation model, i.e. radiation from each parton occurs independently from the structure of the rest of the event, whereas in both HERWIG and PYTHIA radiation is more realistically emitted taking into account color-correlations between all partons in the initial and final state. The output of these Monte Carlo event generators consists of a list of stable particles, which can then be fed to a detector simulation for detailed studies of the expected signature of a top event.

In the pair production process, the t and $\bar{t}$ quarks are produced in the central rapidity region, with P_T of order $M_{top}/2$, (see Fig. 25). These features of $t\bar{t}$ production can be simply understood from the properties of the $i + j \to t\bar{t}$ process. The cross-section for the $q\bar{q} \to t\bar{t}$ subprocess, which dominates at high top mass, is given at lowest order by (see for example Nason, Dawson, and Ellis, 1988) :

$$\hat{\sigma} \ = \frac{8\pi\alpha_s^2}{27\hat{s}}\sqrt{1-\frac{4M_{top}^2}{\hat{s}}}\ \ (1+\frac{2M_{top}^2}{\hat{s}})$$

The parton-parton cross-section as a function of $\hat{s}$ rises from zero at threshold ($\hat{s} = 4M_{top}^2$), reaches a maximum at $\hat{s} = 5.6M_{top}^2$, and then falls off asymptotically as $1/\hat{s}$. When convoluted with the falling $q\bar{q}$ luminosity, (see Fig. 20), the maximum of the $q\bar{q} \to t\bar{t}$ cross-section is shifted down to $\hat{s} \approx 4.5M_{top}^2$. Therefore, the most probable energy for a top quark is E $\approx \sqrt{4.5}M_{top}/2 \approx 1.1M_{top}$, and the most probable momentum is P $\approx 0.4M_{top}$.

From the definition of rapidity, it is clear that the maximum of $|y|$ occurs as $P_T \to 0$ and at maximum E, which for pair-produced objects is $E = 0.5\sqrt{s} = 900$ GeV at the Tevatron. For $M_{top} = 160$ GeV/c^2, the kinematic limit is then $|y| < 2.4$; however, as can be seen from Fig. 25, most top quarks have $|y| < 1.5$. High values of $|y|$ are suppressed because they require $P_T \to 0$, where the phase space factor also $\to 0$, and they require high values of E, i.e. high values of $\hat{s}$. Both the parton-parton luminosities and parton-parton cross-section fall off with increasing $\hat{s}$.

The lowest order diagrams (Fig. 16) lead to a back-to-back topology for the t and the $\bar{t}$ in the transverse plane, which is slightly modified by higher order corrections. Because the top quark momentum is not large compared to M_{top}, the decay products are not significantly boosted along the original top quark flight path, leading to nearly spherical events. In the next Section we will turn to the discussion of top decays and signatures.

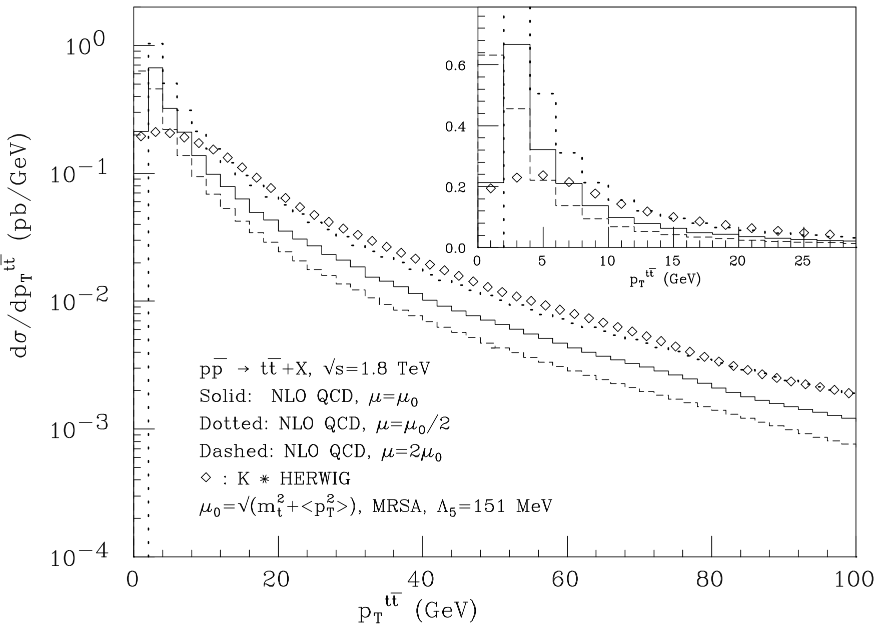

FIG. 26. Comparison of the transverse momentum distributions of the $t\bar{t}$ pair as predicted from the Herwig Monte Carlo and next-to-leading order (NLO) QCD. At Tevatron energies, and for M_{top} = 176 GeV/c^2. From Frixione *et al.*, 1995.

As was mentioned above, shower Monte Carlos are based on the LO matrix element for $t\bar{t}$ production and models of initial and final state radiation. It is interesting to compare these models with higher order QCD calculations. The earlier NLO order calculations of $t\bar{t}$ production (Nason, Dawson, and Ellis, 1988; Beenaker *et al.*, 1991) are not sufficient, since these are calculations of single quark kinematic distributions such as P_T and rapidity, integrated over the whole phase-space for the other quark. More recently, a NLO calculation of the doubly-inclusive cross-section for heavy quark production has become available (Mangano, Nason and Ridolfi, 1992). This calculation allows for comparisons not only of single t or $\bar{t}$ distributions, but also of correlated distributions, e.g. the $t\bar{t}$ invariant mass ($M(t\bar{t})$), the $t\bar{t}$ transverse momentum ($P_T(t\bar{t})$), and the azimuthal separation between t and $\bar{t}$ ($\Delta\phi$). Detailed comparisons between the Herwig model and NLO-QCD have been performed (Frixione *et al.*, 1995). Excellent agreement is found in the shapes of distributions of quark rapidity, P_T, and $M(t\bar{t})$, except for very large values of the latter two quantities. In this kinematic regime, multiple gluon emission from the final state top quarks becomes important, and this process is not modelled by the NLO QCD calculation. Disagreement between NLO QCD and HERWIG is also observed in distributions of $P_T(t\bar{t})$ and $\Delta\phi$, (see Fig. 26). Note that at LO these distributions are delta-functions, with $P_T(t\bar{t}) = 0$ and $\Delta\phi = 180^o$, and deviations from the delta-function behavior are due entirely to higher order corrections. For small $P_T(t\bar{t})$, multiple gluon emission is expected to dominate, and the HERWIG model is expected to be more realistic.

Studies of the expected single top quark P_T and rapidity distributions, calculated in NLO QCD and including the resummation of the leading soft gluon corrections, have also been performed (Kidonakis and Smith, 1995). The shapes of these distributions are found to be essentially identical to those calculated at NLO, which were shown to agree with the Herwig model. Comparisons of gluon emission in $t\bar{t}$ events from HERWIG and from a $O(\alpha_s^3)$ matrix element calculation, including initial and final state gluon radiation have also been made (Orr, Stelzer, and Stirling, 1995). These authors find larger contributions of gluon radiation in HERWIG than in the matrix element calculation. This effect may also be due to the absence of multi-gluon emission in the calculation.

As we will discuss in Section IX, understanding gluon radiation in $t\bar{t}$ events is crucial for a precise determination of the top mass. We expect that this subject will attract more and more attention in the next few years.

V. TOP QUARK SIGNATURES

Since the top quark decays with a very short lifetime, only its decay products can be detected. Therefore, to understand the experimental signature for a top event, we first discuss the decay modes of the top quark. In this Section we review the top quark decay properties and we present a general discussion of how the top quark can be observed, paying particular attention to the background sources. We will concentrate on the signature for $p\bar{p} \to t\bar{t}$, since this is the most important production mechanism at Tevatron Collider energies.

A. Standard Model top quark decay modes

As mentioned in the previous Section, according to the Standard Model the top quark decays as $t \to Wb$, where the W boson is real or virtual depending on the top mass. (Non-Standard Model decay modes of the top quark will be reviewed in Section VI.C). The W will subsequently decay into fermion pairs, either $W \to l\nu$ or $W \to q\bar{q}$, where l denotes a charged lepton, and $q\bar{q}$ denotes a light-quark pair, $u\bar{d}$ or $c\bar{s}$. At tree level, the W couples with equal strength to leptons and quarks, so each W decay mode occurs with equal probability. There are three leptonic channels ($e\nu$, $\mu\nu$, and $\tau\nu$), and six hadronic channels ($u\bar{d}$ and $c\bar{s}$, with three possible color assignments), hence each decay mode has a branching ratio of 1/9. QCD corrections enhance the branching ratios of the hadronic modes by a factor of $(1 + \alpha_s/\pi) \approx 1.05$. Given the W branching fractions, it is a simple matter to list the $t\bar{t}$ decay modes, see Table III.

Decay mode	Branching ratio
$t\bar{t} \to q\bar{q}\ q\bar{q}\ b\bar{b}$	36/81
$t\bar{t} \to q\bar{q}\ e\nu\ b\bar{b}$	12/81
$t\bar{t} \to q\bar{q}\ \mu\nu\ b\bar{b}$	12/81
$t\bar{t} \to q\bar{q}\ \tau\nu\ b\bar{b}$	12/81
$t\bar{t} \to e\nu\ \mu\nu\ b\bar{b}$	2/81
$t\bar{t} \to e\nu\ \tau\nu\ b\bar{b}$	2/81
$t\bar{t} \to \mu\nu\ \tau\nu\ b\bar{b}$	2/81
$t\bar{t} \to e\nu\ e\nu\ b\bar{b}$	1/81
$t\bar{t} \to \mu\nu\ \mu\nu\ b\bar{b}$	1/81
$t\bar{t} \to \tau\nu\ \tau\nu\ b\bar{b}$	1/81

TABLE III. Decay modes for a $t\bar{t}$ pair and their lowest order branching ratios assuming Standard Model decays.

B. Detection of the top decay products

The possible final states contain combinations of electrons, muons, taus, neutrinos, and quarks. Here we briefly illustrate techniques for detection of the top-quark decay products.

General-purpose $p\bar{p}$ collider detectors are needed for top quark physics. These detectors are designed to cover as much as possible of the solid angle around the interaction point, and are composed of a number of sub-detectors optimized for study of different aspects of the event. A number of such detectors have been used (UA1 and UA2 at the CERN S$p\bar{p}$S), are still in operation (CDF and D0 at Fermilab's Tevatron), or are now being designed and constructed (CMS and ATLAS, at the proposed LHC pp collider). While the details of the design of these detectors are different, their overall structure is in general quite similar. The region immediately surrounding the interaction region is instrumented with detectors designed to measure the trajectories of charged particles. Except for UA2 and D0, the tracking volume is immersed in a magnetic field for momentum measurement. The tracking volume is surrounded by calorimeters, where measurements of the energy of electromagnetic and hadronic showers are performed. Calorimeters are segmented both longitudinally and transversely to the direction of flight of particles originating from the interaction point. Transverse segmentation is necessary to measure the position of the showers, while longitudinal information is used to distinguish between electromagnetic (EM) and hadronic (HAD) showers. Calorimeters cover most of the 4π solid angle around the interaction region, however the very forward and backward regions must be left uninstrumented to allow for the passage of the beam pipe. Muon detectors consisting of additional tracking devices, hadron absorbers, and possibly magnets for momentum measurement, are placed outside the calorimeter. Drawings of the two collider detectors at Fermilab's Tevatron are shown in Fig. 27 and Fig. 28.

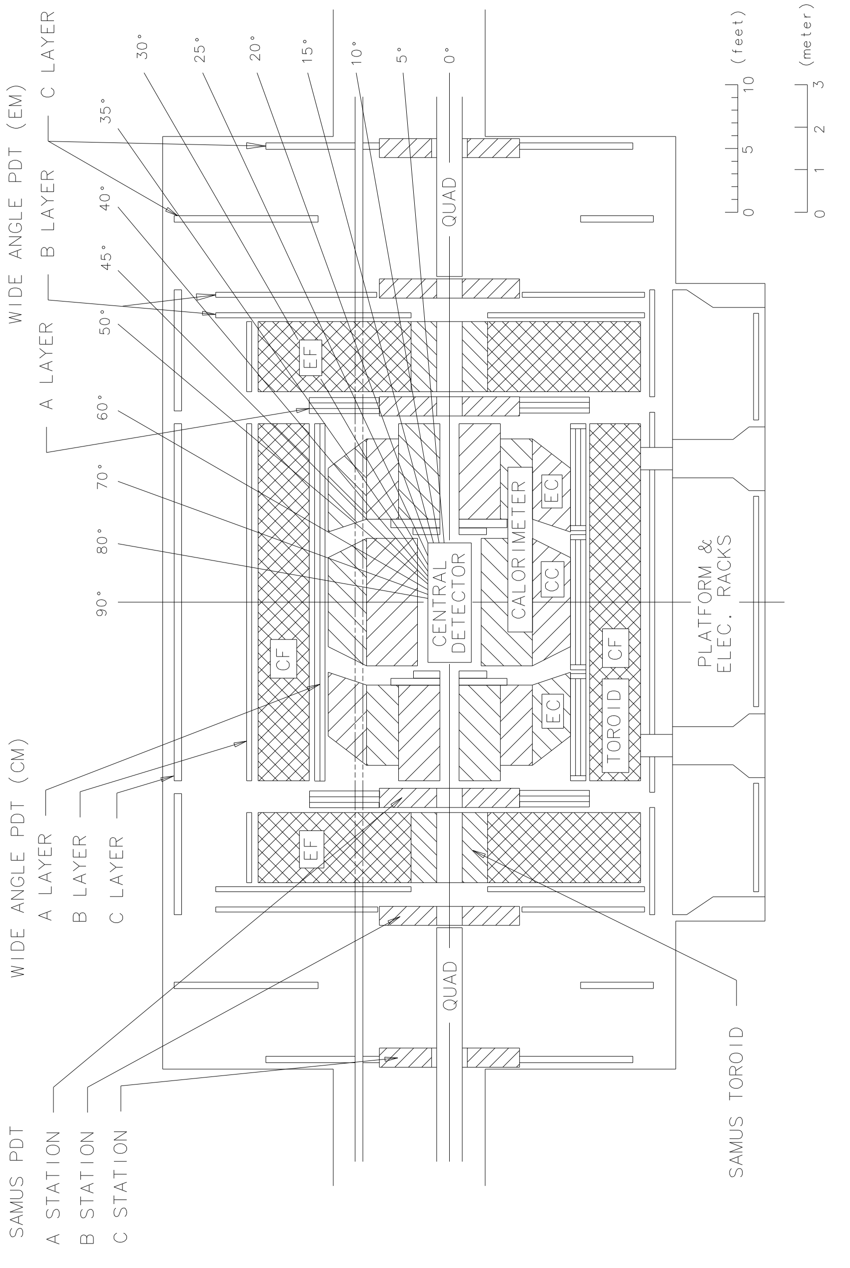

FIG. 27. The D0 detector at the Tevatron. EC and CC are liquid-argon-uranium calorimeters. The central detector provides tracking information. Muons are detected using the five toroids (CF, EF, SAMUS) and the proportional drift tube (PDT) systems, CM and EM. From Snyder, 1995a.

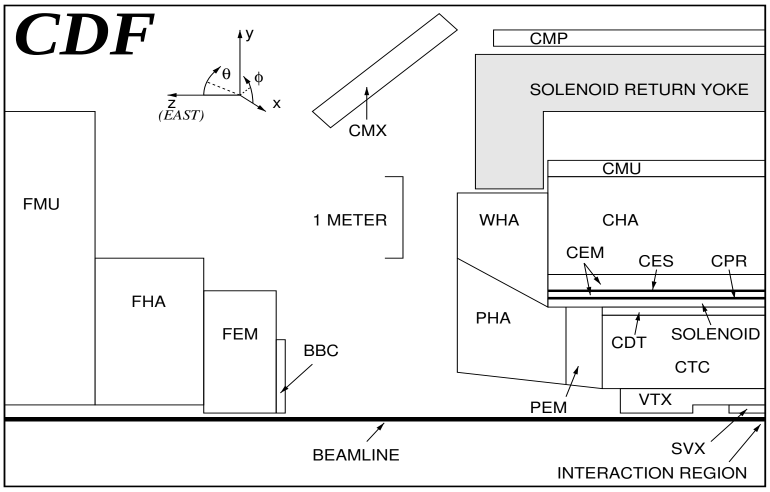

FIG. 28. A side-view cross-section of one quadrant of the CDF detector at the Tevatron. The detector is forward-backward symmetric about the interaction region, which is at the lower-right corner of the figure. SVX, VTX, CTC, and CDT are tracking detectors. CEM, CHA, WHA, PEM, PHA, FEM, and FHA are calorimeters. CMU, CMP, CMX, and FMU are muon detectors. BBC is a bank of scintillators. CPR and CES are multiwire proportional chambers placed in front and in the middle of the central electromagnetic calorimeter (CEM). From F. Abe *et al.*, 1994a.

1. Detection of electrons and muons

Electrons are identified as highly electromagnetic showers in the calorimeters. If momentum information from the tracking system is available, consistency between the measured momentum of the electron candidate and the energy of the corresponding EM-shower provides a powerful handle for rejection of backgrounds from e.g. hadronic shower fluctuations and overlaps between hadron tracks and photons from π^0 decay. Information from the transverse and longitudinal shapes of the shower, from ionization measurements in the tracking chamber (dE/dX), and from the response of transition radiation and preshower detectors, are also used for electron identification.

Electrons from W decays in top events have high transverse momentum, (P_T, see Fig. 29), and are expected to be isolated, i.e. well separated from the other decay products of the two top quarks in a $t\bar{t}$ event. These electrons can be identified with high efficiency, and their energy can be measured very precisely in the calorimeter (see Table IV). On the other hand, identification of electrons from $b \to ce\nu$ in a top event is much more problematic. These electrons have lower transverse momentum than electrons from W decays and, since the b is highly boosted, the nearby hadrons from the b fragmentation and b or c decay may deposit their energy in the same calorimeter cells as these electrons.

Muons can also be reliably identified as charged particles that penetrate the calorimeter and reach the outside muon detectors. Backgrounds to the muon signal arise from decays in flight of pions and kaons, and from hadrons that traverse the calorimeter and hadron absorbers without interacting (*punchthrough*). If there is a magnetic field in the inner tracking system (before the calorimeter), then the muon momentum is precisely measured;

Detector	Electron energy resolution	Muon momentum resolution
UA1	$\sigma(E)/E = (0.15\text{-}0.21)/\sqrt{E} \oplus .03$	$\sigma(P)/P = 0.005P$
UA2	$\sigma(E)/E = 0.17/\sqrt{E} \oplus .02$	-
CDF	$\sigma(E_T)/E_T = 0.14/\sqrt{E_T} \oplus .02$	$\sigma(P_T)/P_T = 0.0009P_T \oplus 0.0066$
D0	$\sigma(E)/E = 0.15/\sqrt{E} \oplus .01$	$\sigma(P)/P = 0.01P \oplus .2$

TABLE IV. Electron energy (GeV) and muon momentum (GeV/c) resolutions in the central region for the UA1 (Albajar *et al.*, 1989), UA2 (Alitti *et al.*, 1992a), CDF (F. Abe *et al.*, 1994a), and D0 (Abachi *et al.*, 1994) detectors. The UA1 muon momentum resolution is for measurements in the central-detector, for muons at 90^o from the direction of the dipole field. The UA1 electron energy resolution changed between 1983 and 1985 due to radiation damage of the scintillator. The symbol $\oplus$ indicates that the two terms are added in quadrature. The subscript T refers to components transverse to the beam direction.

otherwise, (e.g. in the D0 experiment) it is measured, with worse resolution, in the outer muon detector (see Table IV).

2. Detection of quarks

Quarks hadronize and are detected as collimated *jets* of particles, (see Fig. 30). Jets in $p\bar{p}$ collisions are reconstructed by summing up the energy deposited in the calorimeter cells within a fixed cone in $\eta-\phi$ space, where η is the pseudorapidity, and ϕ is the azimuthal angle around the beamline. The fixed cone algorithm is used because jets are are approximately *circular* in $\eta-\phi$ space, because the $\eta-\phi$ size of a jet of a given P_T is independent of the rapidity of a jet, and because this size is only weakly dependent on the transverse momentum of the jet, as we will briefly discuss below.

If the typical longitudinal and transverse momentum components of a fragmentation particle with respect to the jet axis are q_T and q_l, then the typical spread of the jet will be $\Delta\theta \approx q_T/q_l$ and $\Delta\phi \approx q_T/(q_l \sin\theta)$, for $q_T << q_l$. Then, $\Delta\eta = (d\eta/d\theta)\ \Delta\theta \approx -q_T/(q_l \sin\theta) = -\Delta\phi$, i.e. jets are approximately circular in $\eta-\phi$ space. Since the rapidity of a massless particle under a longitudinal boost changes as $y \rightarrow y + \Delta y$, where Δy only depends on the boost, in the limit that the mass of the fragmentation hadrons is small, the η size of a jet of a given P_T is invariant under longitudinal boosts, i.e. independent of the η of the jet itself. The size of a jet does vary slightly with its transverse momentum; for example a simple model of jet fragmentation uniform in rapidity along the jet axis predicts that the angular size of the cone containing half of the particles in the jet varies as $1/\sqrt{E}$, where E is the energy of the jet.

The size of the cone used in jet reconstruction must be matched to the size of a jet. On average, of order 70% of the jet energy is contained within a cone of radius $\Delta R = \sqrt{\Delta\eta^2 + \Delta\phi^2} = 0.4$ (F. Abe *et al.*, 1991c and 1993a; Linneman, 1995.). See also Fig. 31; NB: $\Delta R < 0.4$ translates into $\Delta\phi < 23^o$ in Fig. 31.

The energy of a jet is defined as the energy of the corresponding calorimeter cluster. The resolution in the measurement is typically only of order $\sigma(E_T)/E_T \approx 1.0/\sqrt{E_T}$ (E_T in GeV),

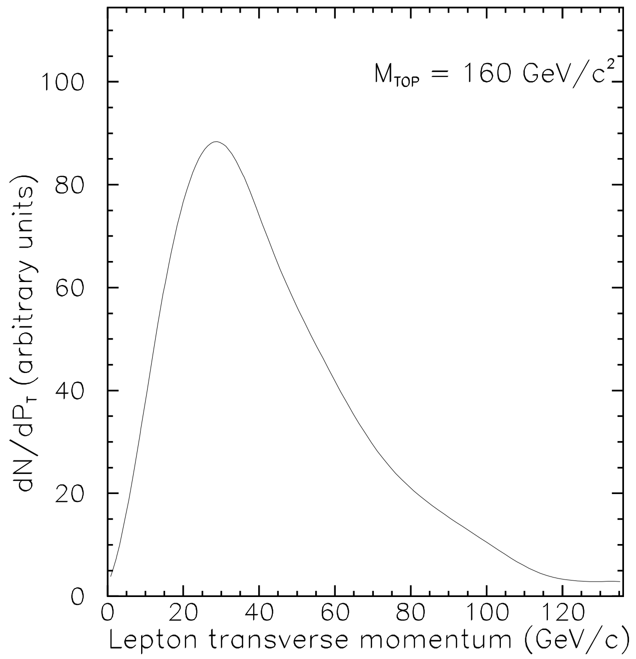

FIG. 29. The expected lepton transverse momentum from $t \to Wb \to l\nu$ from the ISAJET Monte Carlo generator. This is for $p\bar{p} \to t\bar{t}$ at $\sqrt{s} = 1.8$ TeV. Detector effects are not included.

(see Fig. 32). This poor resolution is due to (i) the intrinsic large fluctuations in the response of calorimeters to hadronic showers, (ii) differences in the calorimeter response between charged hadrons and electrons or photons, (iii) energy loss in uninstrumented calorimeter regions, e.g. in the vicinity of boundaries between calorimeter modules, (iv) energy loss due to the use of a finite cone-size in jet reconstruction, and (v) overlaps between the jet and hadrons from the underlying event. The direction of a jet is measured by linking the position of the energy cluster in the calorimeter with the position of the interaction point. The resolution on the angular measurement is a few degrees.

The number of detected jets for a given decay mode in a $t\bar{t}$ event is not expected to correspond to the number of quarks in the final states listed in Table III. There are a number of reasons for this. First, as the P_T of the parton becomes small, identification of the corresponding jet becomes more and more problematic, as it tends to blend with the underlying event. In practice, one imposes a minimum cutoff on the jet transverse momentum which is set to a value at least of order 10 GeV/c. Furthermore, as will be discussed further in this Section, backgrounds to the top signal consist mainly of events with low P_T jets. Therefore, to achieve the needed background rejection, the minimum jet P_T requirement is often chosen to be higher than 10 GeV/c. A second source of jet reconstruction inefficiency is jet merging. Nearby jets can be resolved only if their separation in $\eta - \phi$ space is larger than a minimum distance of the order of the clustering radius used in jet reconstruction. Top events have a large number of partons in the final state, and the probability that at least two of them will be too close to be separately identified is substantial. In those cases, the two nearby jets are merged and are reconstructed as a single jet.

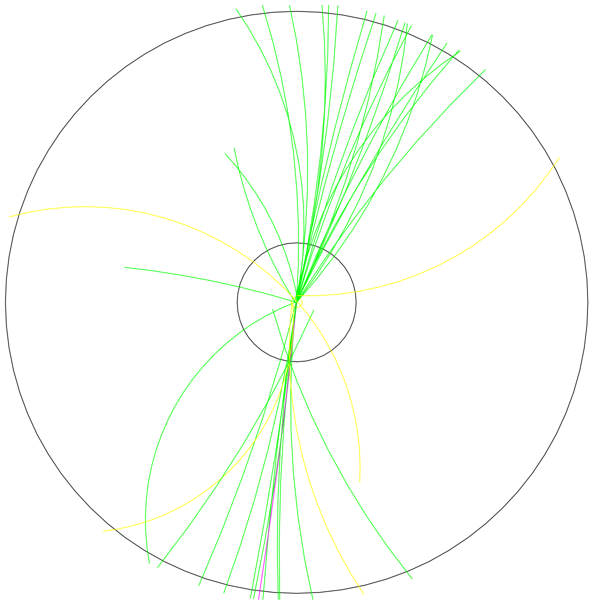

FIG. 30. A $p\bar{p} \to$ jet-jet event in CDF. Here we show the reconstructed tracks in the transverse plane. The *two-jet* structure is apparent.

To illustrate some of these effects, we show in Fig. 33 the expected transverse momenta and separation (ΔR) in $\eta - \phi$ space for quarks in $t\bar{t} \to q\bar{q}\ l\nu\ b\bar{b}$ events for $M_{top} = 170$ GeV/c^2. Different experiments and different analyses use different cone clustering radii, typically between 0.3 and 1.0. In a significant fraction of events, the minimum ΔR between quarks is small enough that at least two of the quark-jets are expected to be merged. Even for a high top mass, the fraction of events with at least one relatively soft jet is substantial (again, see Fig. 33). For lower top masses of course the transverse momenta will be even lower. The situation for M_{top} close to M_W is particularly difficult. In that case the kinetic energy liberated in the $t \to Wb$ decay is low and the b momentum in the top rest frame is small. Even after boosting to the laboratory frame, the b momentum remains soft, (see Fig. 34).

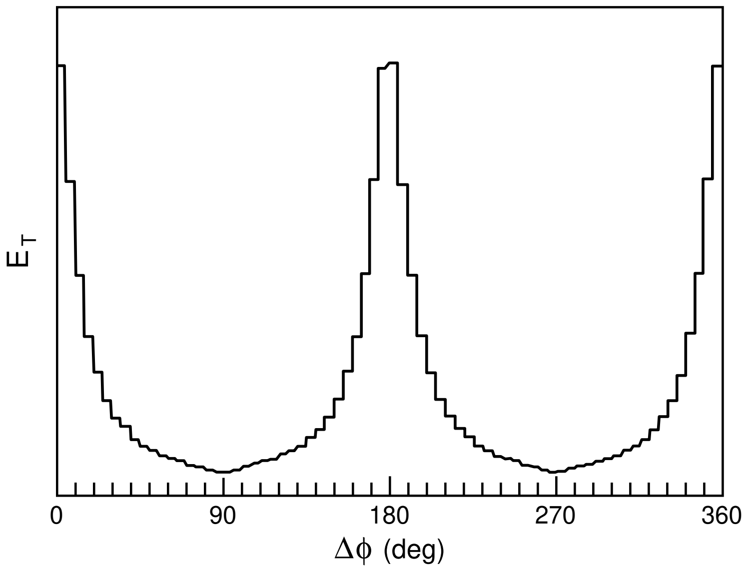

FIG. 31. The relative E_T distribution in calorimeter cells at an angle ϕ with respect to the transverse jet thrust axis for CDF di-jet data with a 30 GeV E_T jet trigger threshold. Note that in these di-jet events one jet is at $\phi = 0^o$, and the other jet is at $\phi = 180^o$. From F. Abe *et. al*, 1991c.

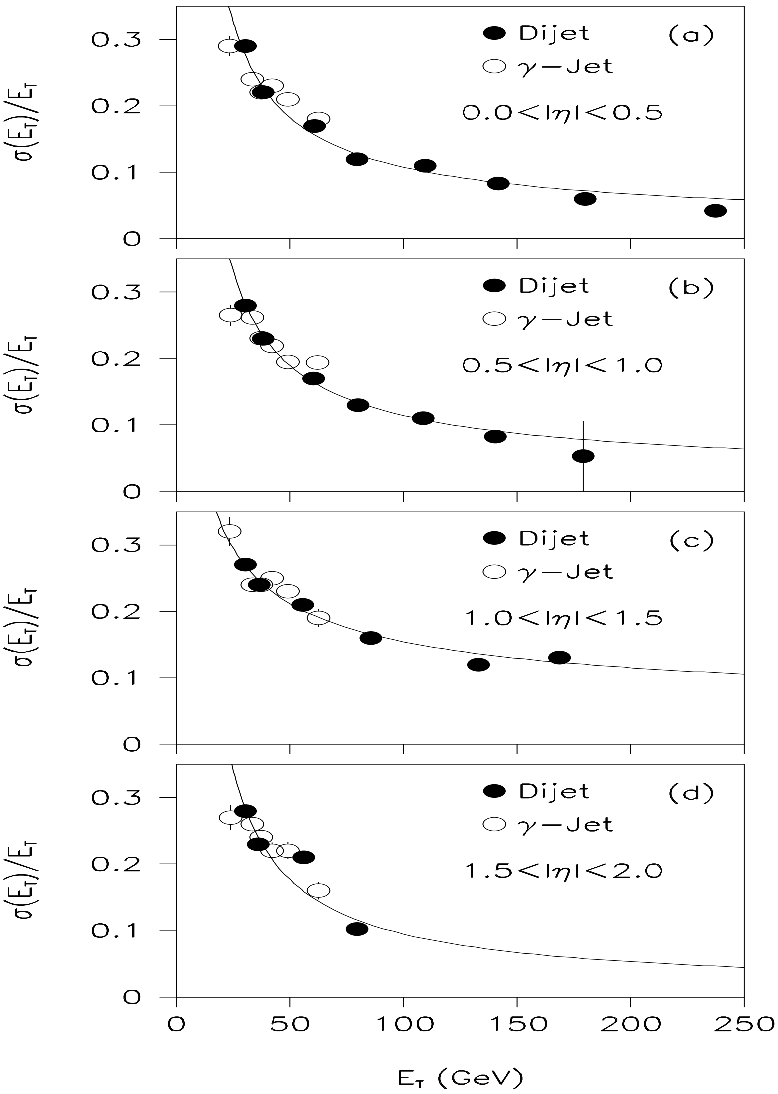

FIG. 32. From the D0 experiment, Abachi 1995d; jet energy resolution as a function of jet transverse energy (E_T) as computed from di-jet and photon-jet events in four pseudo-rapidity regions. The fits are of the form $(\sigma_E/E)^2 = (N/E)^2 + (S/\sqrt{E})^2 + C^2$. The fitted values of N, S, and C are : (a) $N = 7.07$, $S = 0.81$, $C = 0.0$; (b) $N = 6.92$, $S = 0.91$, $C = 0.0$; (c) $N = 0.0$, $S = 1.45$, $C = 0.052$; (d) $N = 8.15$, $S = 0.48$, $C = 0.0$. Jets are reconstructed using a cone-size of 0.5.

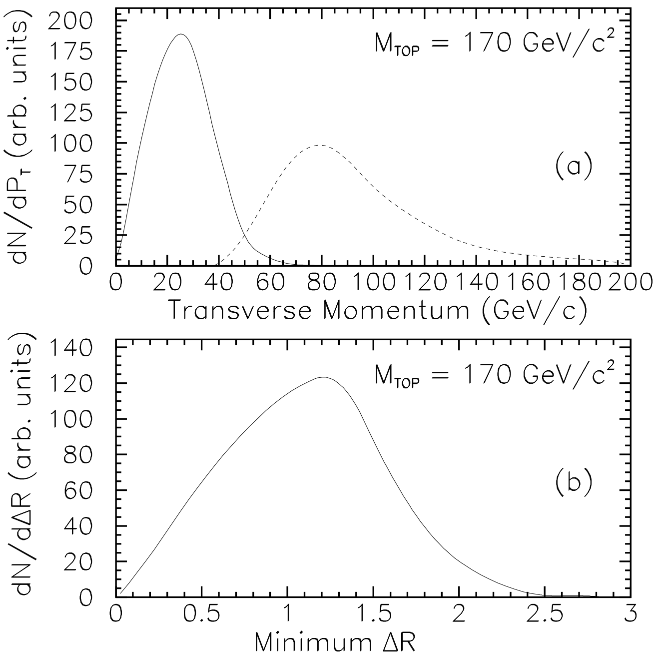

FIG. 33. (a) The expected transverse momentum of the lowest (solid) and highest (dashed) P_T quark in lepton + jets events; (b) ΔR between the closest two quarks in $p\bar{p} \rightarrow t\bar{t} \rightarrow q\bar{q}\ l\nu\ b\bar{b}$. Results are from the ISAJET Monte Carlo event generator at $\sqrt{s} = 1.8$ TeV. Detector effects are not included.

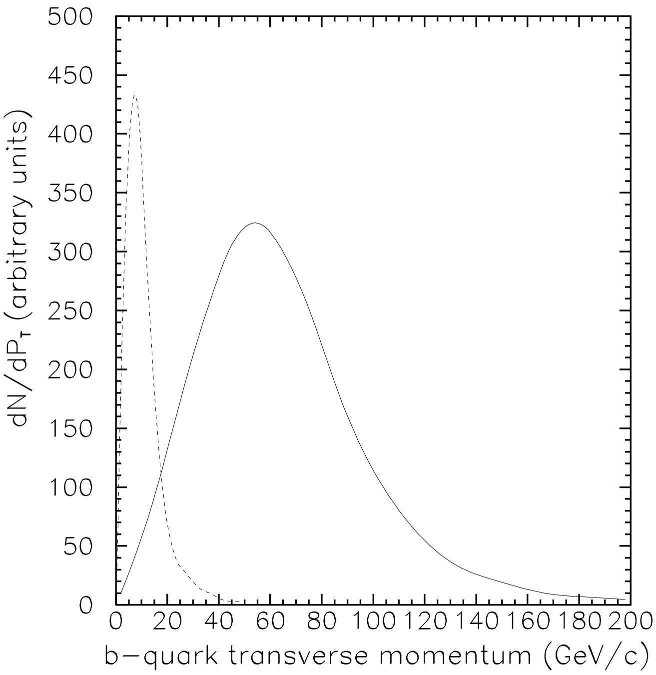

FIG. 34. The expected transverse momentum distribution of b-quarks from top decay for M_{top} = 170 GeV/c^2 (solid) and M_{top} = 90 GeV/c^2 (dashed). Results are from the ISAJET Monte Carlo event generator for the process $p\bar{p} \rightarrow t\bar{t}$ at $\sqrt{s} = 1.8$ TeV. Detector effects are not included.

The situation gets even more complicated when initial and final state radiation are taken into account. Initial state gluon radiations gives a net P_T to the $t\bar{t}$ system, and therefore alters the jet P_T spectrum calculated at tree-level; the radiated gluons can be detected as additional jets in the final state; large angle radiation from the final state quarks softens the spectrum of reconstructed jets, and can also result in additional jets.

All of these jet reconstruction effects are important, and must be studied using QCD-inspired Monte Carlo event generators, in conjunction with a simulation of the detector response, see for example Fig. 35. They constitute one of the major systematic uncertainties in the calculation of the $t\bar{t}$ acceptance and, more importantly, in the determination of the top mass, see Section IX.

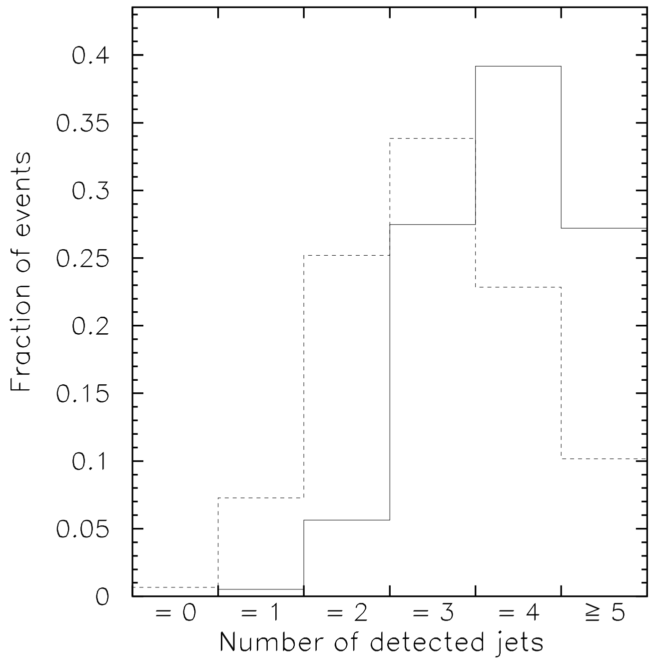

FIG. 35. Jet multiplicity in $t\bar{t} \to l\nu bq\bar{q}b$ (lepton + jets) events from the ISAJET Monte Carlo and the CDF detector simulation. Solid line : M_{top} = 200 GeV/c^2; dashed line : M_{top} = 120 GeV/c^2. Jets are reconstructed using a cone-size ΔR=0.4, and must have $|\eta| < 2$. The jet transverse energy threshold is 15 GeV, without application of jet energy corrections. (The jet energy corrections will be described in Section IX.A.3; a 15 GeV jet in CDF is corrected on average to $\approx$ 23 GeV). Note that in the absence of gluon radiation these events should have $N_{jets} \leq 4$; the significant fraction of events with additional jets in the final state is an indication of the importance of gluon radiation.

3. Detection of neutrinos

Neutrinos are detected by missing momentum techniques: since the initial center-of-mass momentum is zero, the vector sum of the momenta of all of the neutrinos in the event is inferred as the negative of the vector sum of the momenta of all the detected particles. However, because the very forward and backward detector regions are uninstrumented, longitudinal information is lost, and only the transverse components of the momenta of neutrinos

Detector	$\sigma(\not{E}_{\mathrm{T}})$	Reference
UA1	$0.7\ \sqrt{\Sigma E_T}$ (in GeV)	Albajar *et al.*, 1989
UA2	$0.8\ (\Sigma E_T)^{0.4}$ (in GeV)	Alitti *et al.*, 1990b
CDF	$0.7\ \sqrt{\Sigma E_T}$ (in GeV)	F. Abe *et al.*, 1994a
D0	1.08 GeV $+ 0.019\ \Sigma E_T$	Abachi *et al.*, 1995d

TABLE V. Missing transverse energy resolution for minimum bias events.

can be measured. In practice, what is measured is not the momentum of all of the particles, but rather the energy deposited in the calorimeter. The missing transverse energy vector ($\vec{\not{E}}_{\mathrm{T}}$) is defined as $\vec{\not{E}}_{\mathrm{T}} \equiv -\Sigma_i \vec{E_T^i}$, where the sum is over all calorimeter cellss, and $\vec{E_T^i}$ is a vector whose direction points to the *ith* cell and whose magnitude is equal to the transverse energy deposited in the *ith* tower. The missing transverse energy vector must be corrected for detected muons which only loose a minimal amount of energy in the calorimeter, and is then associated with the neutrino transverse momentum.

The resolution on the neutrino energy measurement is very much dependent on the event topology, since it depends directly on the resolution in the measurements of all the leptons and jets in the event. Since leptons are in general well measured, the uncertainty in the measurement of $\not{E}_{\mathrm{T}}$ arises mostly from errors in the measurements of jet energies. It is customary to parametrize the resolution in $\not{E}_{\mathrm{T}}$, $\sigma(\not{E}_{\mathrm{T}})$, as a function of the total transverse energy in the event, ΣE_T, see Table V.

4. Detection of tau leptons

Taus are very hard to identify. Approximately 36% of the time, a tau lepton will decay into a muon or an electron. The signature for an event with a $t \to W \to \tau\nu \to l\nu\nu$, where $l = e$ or μ, is very similar to that of an event with a $t \to W \to l\nu$ decay, except that the final state lepton will in general have lower momentum. Taus that decay hadronically are detected as jets. Separation between jets from hadronic decays of taus and quarks or gluon jets in $p\bar{p}$ collisions has been achieved in e.g. measurements of the $p\bar{p} \to W \to \tau\nu$ cross-section (Albajar *et al.*, 1989; Alitti *et al.*, 1991b; F. Abe *et al.*, 1992b), and in searches for non Standard-Model top quark decays, see Section VI.C. The separation is based on the distinctive narrowness of a jet from the hadronic decay of a high P_T tau-lepton, and/or the characteristic one- and three-prong track multiplicities. However, the efficiency for detecting hadronic taus is so low, and the backgrounds from jet fluctuations are so high, that these techniques are only now just beginning to be applied successfully in the context of a Standard Model top search.

For the remainder of this article, we will refer to $t\bar{t}$ final states with zero, one, or two leptons (e or μ) from W decay as *all hadronic, lepton + jets*, and *dilepton* respectively. Signatures that include the explicit identification of hadronic tau-decays will not be considered in this review. We now turn to a discussion of the $t\bar{t}$ signatures in these three channels.

C. All hadronic mode

The all hadronic final state, ($t\bar{t} \to q\bar{q}\ q\bar{q}\ b\bar{b}$, see Table III) is the most common, but it competes with very high backgrounds from $p\bar{p} \to 6$ jets (see for example Benlloch, Wainer, and Giele, 1993). The cross-sections for this QCD process at the Tevatron is higher than the top cross-section by approximately three orders of magnitude. Despite the extremely high background levels, it may be possible, with sufficient statistics, to isolate a top signal in this mode by applying further kinematic cuts, and by identifying the b-quark(s) in the final state. These issues are being carefully studied by the experimenters (Castro, 1994; Tartarelli, 1996; Narain 1996). In this review we will concentrate on the dilepton and lepton + jets modes.

D. Dilepton mode

The signature for the dilepton final state ($t\bar{t} \to l\nu\ l\nu\ b\bar{b}$, see Table III) consists of two leptons, two b-jets, and $\not{E}_{\rm T}$ from the two neutrinos. Since the leptons originate from W decay, they tend to be isolated and to have high transverse momenta. The $\not{E}_{\rm T}$ is also expected to be high, (see Fig. 36). Typical minimum lepton transverse momentum or $\not{E}_{\rm T}$ requirements are set around 20 GeV/c. Despite the low branching ratio, this mode turns out to be very important because background levels are very low.

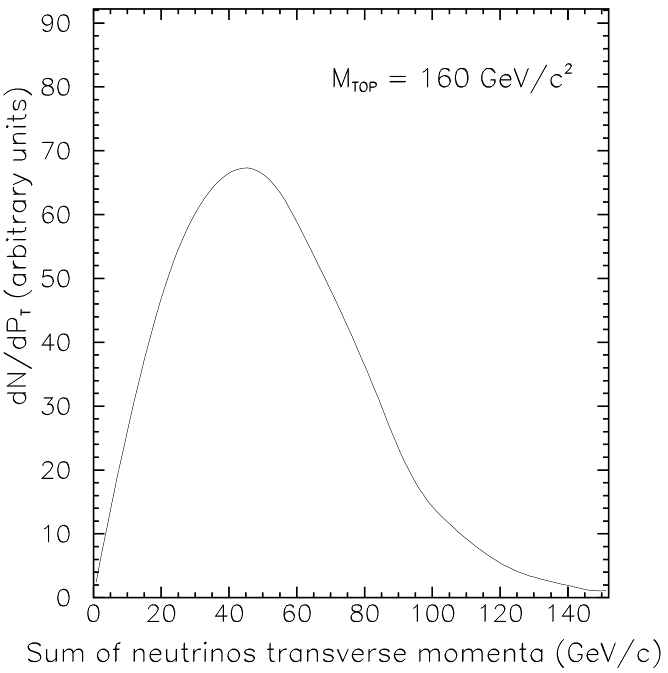

FIG. 36. Expected sum of neutrinos' transverse momenta in the dilepton channel ($p\bar{p} \to t\bar{t} \to l\nu b l\nu\bar{b}$) at $\sqrt{s} = 1.8$ TeV. From the ISAJET Monte Carlo event generator, for $\mathrm{M}_{top} = 160$ GeV/c^2.

The most probable way to obtain two isolated leptons in $p\bar{p}$ collisions is through the Drell-Yan process, see Fig. 37. This mechanism yields e^+e^- and $\mu^+\mu^-$ pairs, but not $e\mu$

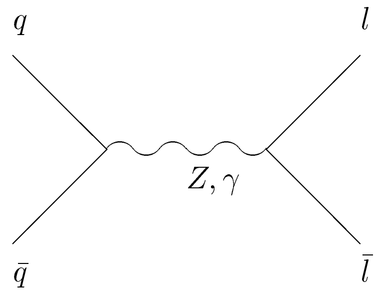

FIG. 37. Lowest order Feynman diagram for Drell-Yan production of lepton pairs.

pairs, except through $\tau\tau$ production, with both taus decaying leptonically. Here we begin by addressing backgrounds from direct Drell-Yan production of ee and $\mu\mu$ pairs.

The dominant Drell-Yan $p\bar{p} \to Z \to l^+l^-$ resonance can be easily eliminated by a l^+l^- invariant mass cut, with a modest (≈ 25 %) loss in top acceptance. After the Z removal, the rate of high transverse momentum Drell-Yan pairs is still approximately two orders of magnitude higher than the $t\bar{t}$ dilepton rate (for $\mathrm{M}_{top} \approx 150$ GeV/c^2). Additional background rejection can be obtained because (i) in Drell-Yan events there are no additional emitted jets at lowest order, and (ii) there are no neutrinos, and hence zero $\not{E}_{\mathrm{T}}$ except for resolution effects. Higher order QCD corrections to the diagram shown in Fig. 37 give rise to final state jets, for example from gluons radiated off the q and $\bar{q}$ lines. For each additional jet, the rate is reduced by a factor of $\mathrm{O}(\alpha_s) \approx 0.15$. Since there are two b-quark jets in $t\bar{t}$ dilepton events, one can achieve a significant background rejection factor, while maintaining efficiency for top, by demanding that at least two jets be detected in addition to the l^+l^- pair. In conjunction with a $\not{E}_{\mathrm{T}}$ requirement, the Drell-Yan background can then be reduced to a tenth or less of the expected top signal for top masses as high as 200 GeV.

As was mentioned above, Drell-Yan $\tau\tau$ production, followed by leptonic decays of both taus ($\tau \to l\nu\nu$), constitutes an additional source of lepton pairs. Events from the $Z \to \tau\tau$ resonance cannot be easily removed because the invariant mass information is lost due to the presence of four neutrinos in the final state. However, the transverse momenta of the leptons and the $\not{E}_{\mathrm{T}}$ for these events are significantly lower than in $t\bar{t}$ dilepton events, (see Figs. 38, 29, and 36). By requiring high transverse momentum leptons, high $\not{E}_{\mathrm{T}}$, and two jets, this background can be reduced to approximately the same level as the ee and $\mu\mu$ Drell-Yan background. We note here that, unlike in the case of direct Drell-Yan production of ee and $\mu\mu$ pairs, this process can result in $e\mu$ final states.

Diboson production, (see Fig. 39), constitutes an additional source of high P_T dileptons and $\not{E}_{\mathrm{T}}$. These are exceedingly rare processes, which are extremely interesting in their own right. The cross-section for WW production has been calculated to next-to-leading order, and at $\sqrt{s} = 1.8$ TeV it is estimated to be $\sigma(WW) \approx 10$ pb (Ohnemus, 1991a). This is the same as $\sigma(t\bar{t})$, for $\mathrm{M}_{top} \approx 160$ GeV/c^2. When both W-bosons decay leptonically, the kinematics for the leptons and the neutrinos are very similar as those expected from $t\bar{t}$, which also results in a WW pair in the final state. The most efficient method that can be used suppress this background is to require that there be jets in the event. Just as in the Drell-Yan process, there are no jets at leading order in WW events. By demanding that there be two jets, the background is reduced by a factor of order $\alpha_s^2 \approx 0.02$. Backgrounds from WZ and ZZ production are smaller by over one order of magnitude because (i) the

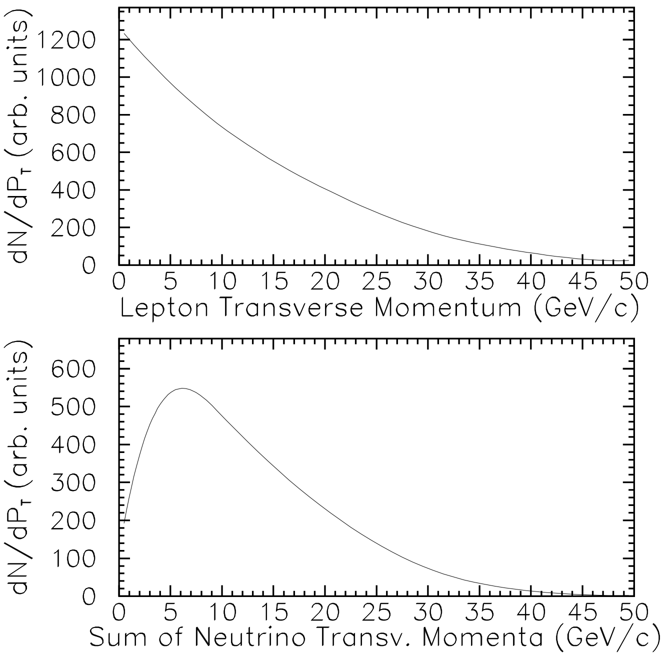

FIG. 38. The expected lepton and neutrino transverse momenta in $p\bar{p} \to Z \to \tau^+\tau^-$, $\tau^+ \to l^+\nu\nu$, $\tau^- \to l^-\nu\nu$ at $\sqrt{s} = 1.8$ TeV. From the ISAJET Monte Carlo generator.

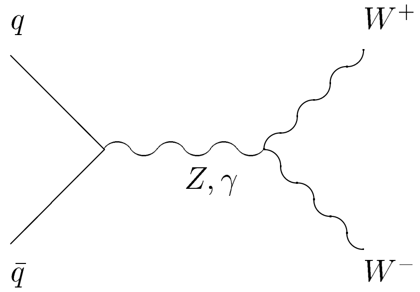

FIG. 39. Lowest order Feynman diagram for production of WW pairs in $p\bar{p}$ collisions; similar diagrams lead to WZ and ZZ production.

WZ and ZZ production cross-sections are significantly lower than that of WW (Ohnemus, 1991b; Ohnemus and Owens, 1991), (ii) the leptonic branching ratios of the Z are a factor of three smaller than those of the W, and (iii) l^+l^- pairs from Z decays can be eliminated with an invariant mass cut.

Additional backgrounds to the dilepton signal from fake leptons as well as doubly-semileptonic decays of $b\bar{b}$ pairs also have to be considered, but are generally found to be small. In a given analysis the signal-to-background level can be tuned by the choice of requirements. In general, raising the minimum P_T cut on the jets eliminates more background events than signal events. The reason for this is that for sufficiently high M_{top} the P_T spectrum of b-jets in dilepton top events is harder than the brehmstrahlung-like spectrum of jets in all the processes listed above. Higher $\not{E}_T$ or lepton P_T requirements would considerably lower all backgrounds except the diboson background; the $Z \to \tau\tau$ background could be entirely eliminated by requiring the invariant mass of the l^+l^- pair to be higher than the Z

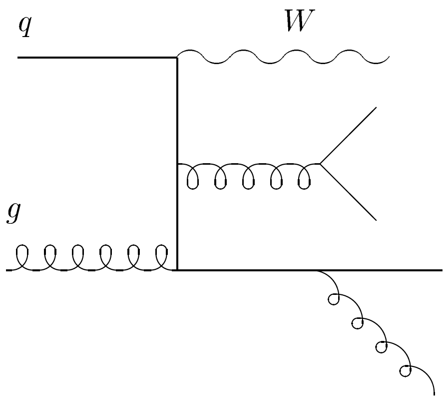

FIG. 40. Feynman diagram for $W+$ 4 jet production in $p\bar{p}$ collisions. Many other diagrams also contribute.

mass; requiring that jets be b-tagged would reduce all backgrounds by about two orders of magnitude. With sufficient luminosity, it should be possible to obtain very pure $t\bar{t}$ samples in the dilepton mode.

E. Lepton + jets mode

The branching ratio for this mode ($t\bar{t} \to q\bar{q}l\nu b\bar{b}$) is quite large, 24/81, see Table III. The signature consists of one isolated, high P_T lepton (e or μ), $\not{E}_T$ from the neutrino, two light quark jets (u, d, c, or s), and two b-quark jets.

As was discussed in Section V.B.2, in practice the number of detected jets is not expected to be always four. In order to maintain high efficiency, in most analyses the number of jets requirement is usually relaxed to ≥ 2 or ≥ 3, except for very high top mass, or where detection of a fourth jet is essential, e.g. for the determination of the top mass, see Section IX.

1. $W+$ jets background

For sufficiently high top mass, the dominant background to $t\bar{t}$ in the lepton + jets channels is due to W + multijets production, (see Fig. 40). The inclusive W production cross-section at the Tevatron is $\sigma(p\bar{p} \to W) \approx 20$ nb, over three orders of magnitude higher than the $t\bar{t}$ cross-section for $M_{top} > 150$ GeV/c^2. The cross-section for $W+$ N jets is suppressed by factors of order α_s^N.

Other backgrounds, such as $p\bar{p} \to b\bar{b}$ + jets followed by $b \to cl\nu$, and backgrounds from fake leptons also need to be carefully evaluated. For top masses above ≈ 40 GeV/c^2, where an efficient lepton + jets top selection can be devised based on **both** a high P_T lepton and high missing transverse energy, these backgrounds are in general found to be much smaller.

The importance of the W + multijets process as a background to top production, as well as to more exotic phenomena (e.g. supersymmetry), was noted soon after the first results from the S$p\bar{p}$S collider became available. As a result, a large theoretical effort was directed towards the calculation of the cross-sections and kinematic properties for $p\bar{p} \to W$ (or Z) + N jets. The first calculations, for N=1 or 2, were performed in the mid-eighties (Ellis and Gonsalves, 1985; Ellis, Kleiss, and Stirling, 1985; Kleiss and Stirling, 1985; Gunion and

Kunstz, 1985). These were then extended to final states with 3 (Berends, Giele, and Kuijf, 1989; Hagiwara and Zeppenfeld, 1989) and 4 jets (Berends *et al.*, 1991).

These calculations are performed at tree-level, and therefore they diverge as the angular separation between outgoing partons becomes very small or as their transverse momenta tend to zero (*collinear* and *infrared* divergences). However, far enough away from the regions of divergence, calculations are expected to be quite reliable, within the estimated theoretical uncertainties due to the missing higher order terms. Agreement is found between the measured W + jets cross-section and the theoretical prediction, (see Fig. 41). The degree of confidence in these LO calculations is such that the theoretical predictions have been used to extract the value of α_s from the $W+$ jet data (Lindgren, 1992; Alitti *et al.*, 1991c). More recent measurements of α_s (Abachi *et al.*, 1995c) have been based on the full NLO (order α_s) calculation for $p\bar{p} \rightarrow W$ (Giele, Glover, and Kosower, 1993).

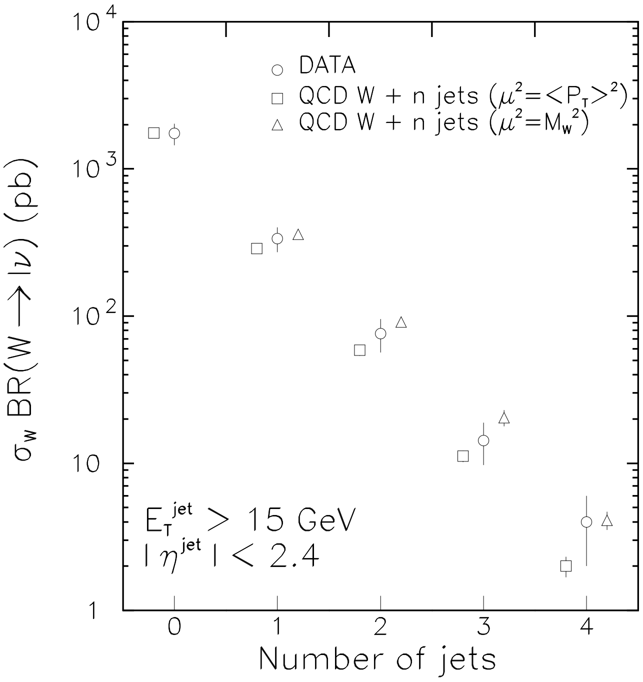

FIG. 41. Product of W cross-section (σ_W) times leptonic branching ratio as a function of jet multiplicity in $p\bar{p}$ collisions at $\sqrt{s} = 1.8$ TeV. The LO QCD predictions are shown for two different choices of the renormalization and factorization scale μ. The jet E_T threshold was set at 15 GeV. From F. Abe *et al.*, 1993b.

The LO theoretical calculation for $p\bar{p} \rightarrow W$ (or Z) + N jets, for N up to 4, is implemented in the VECBOS Monte Carlo event generator (Berends *et al.*, 1991), which is extensively used by the experimenters to model the W + jets background. VECBOS is a parton-level Monte Carlo generator, i.e. its output consists of parton four-vectors only. In order to properly simulate the response of the detector, hadronization effects are included by interfacing the VECBOS event generator with hadronization models based e.g., on independent parton-fragmentation (Field and Feynman, 1978), or the HERWIG model (Marchesini and Webber, 1984 and 1988). A model of the underlying event also needs to be included.

In what follows we will show several comparisons of theoretical expectations for $t\bar{t}$ and

$W+$ jets at Tevatron energies. These comparisons are performed at the parton-level only, i.e. hadronization, as well as detector effects, such as resolution smearing, efficiencies etc., are not included. Therefore, the discussion presented here is intended only as a general illustration of the issues involved.

The two processes are modeled with the ISAJET (for $t\bar{t}$) and VECBOS (for $W+$ jets) event generators. The ISAJET model employed here does not include initial and final state gluon radiation effects; the $t\bar{t}$ rates are normalized to a recent $p\bar{p} \to t\bar{t}$ cross-section calculation (Laenen, Smith, and van Neerven, 1994). In order to mimic actual experimental conditions, and to avoid the infrared and collinear divergencies in the $W+$ jets calculation, we impose the following requirements :

- P_T of partons (quarks or gluons) > 15 GeV/c
- $|\eta|$ of jets < 2
- P_T of leptons (electrons, muons and neutrinos) > 20 GeV/c
- $|\eta|$ of electron or muon < 1
- ΔR between jets > 0.5

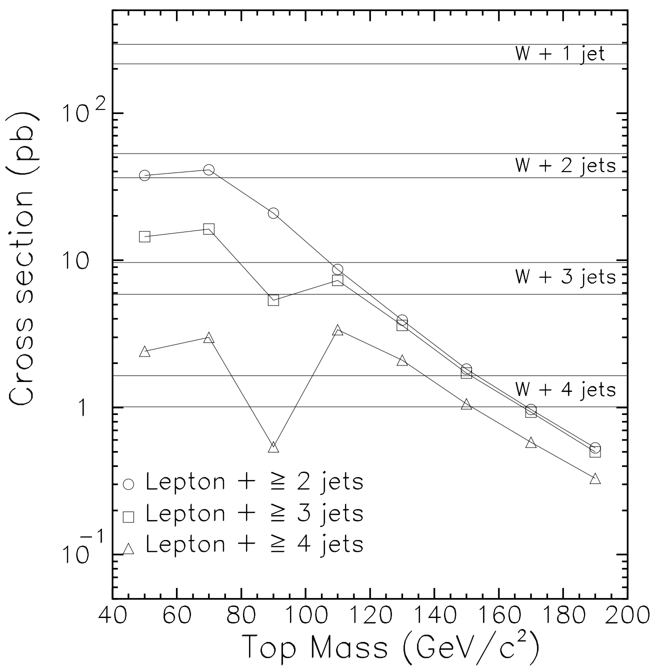

FIG. 42. Comparison of expected lepton + jets rates at the Tevatron for $t\bar{t}$ and $W+$ jets as a function of jet multiplicity and top mass. Detector and $t\bar{t}$ gluon radiation effects are not included. The $W+$ jets theoretical predictions are given as bands which reflect the effects of reasonable variations in the μ^2 scale. See text for details.

In Fig. 42 we show the expected rates of lepton + jets events from $t\bar{t}$ and $W+$ jets. (To get a feeling for the effects of gluon radiation, which are not included here, see for example

Fig. 35). Note the drop in efficiency for detecting a fourth jet in $t\bar{t}$ events, even at top masses of 200 GeV. As discussed in Section V.B.2, this is due to (i) final state quarks having P_T below the threshold (15 GeV/c in this case), and (ii) to the effect of jet merging. The expected signal-to-background, for a lepton + $\geq$ 3 jets selection, with a 15 GeV jet P_T threshold, varies between about 1/1 at M_{top} = 100 GeV/c^2 and 1/10 at M_{top} = 200 GeV/c^2. By requiring $\geq$ 4 jets, the signal-to-background for high top quark mass is significantly improved (by approximately a factor of 3 for M_{top} = 200 GeV/c^2). As we will show, further improvements in signal-to-background can be achieved by raising the P_T threshold on the jets. For top masses in the neighborhood of the W-mass, b-quarks are expected to have a soft transverse momentum spectrum, (see Fig. 34). As a result, the probability of detecting more than two jets in this mass region is particularly low. The required number of detected jets in a lepton + jets top search is therefore in general dependent on the top mass region that is being explored.

The cross-section for $W+$ N jets is proportional to α_s^N, therefore for each additional jet the W cross-section drops by a factor of order α_s. The $W+$ jets predictions in Fig. 42 are derived from VECBOS, which is based on a tree-level calculation with significant uncertainties. These uncertainties can be partially quantified by the stability of the calculation under changes in the factorization and renormalization scale μ. Here we present these predictions as bands that reflect the variation between the choices $\mu^2 = M_W^2$ and $\mu^2 =< P_T >^2$, where $< P_T >$ is the average transverse momentum of the partons in the event.

The relative uncertainty on the $W+$ N jets cross-section due to the choice of μ grows with the number of jets. This is because $\sigma(W+$ N jets) is proportional to $\alpha_s^N(\mu^2)$, so that when choosing a different μ^2, $\delta\sigma/\sigma$ becomes proportional to N $\delta\alpha_s/\alpha_s$ (where we have ignored the μ^2 dependence of the parton distribution functions that need to be convoluted with the partonic cross-section).

Because of these theoretical uncertainties, the existence of the top quark cannot be firmly established based on just the observation of an excess of $W+$ jets events. Additional information need to be employed to isolate a potential top signal. A number of possibilities will be discussed next.

2. Separation of $W+$ jets and $t\bar{t}$ for $M_{top} < M_W + M_b$

As discussed previously, if $M_{top} < M_W + M_b$, the W from the decay $t \rightarrow Wb$ will be virtual (W^*). In this case, the invariant mass of the $l\nu$ pair in $t\bar{t}$ events from $W^* \rightarrow l\nu$ will be smaller than both M_W and M_{top}. In contrast, the $l\nu$ pair in $W+$ jets events, which originates from real W decays, has invariant mass equal to the W mass. However, as was mentioned in Section V.B.3, the longitudinal component of the neutrino momentum cannot be measured, so the $l\nu$ invariant mass cannot be calculated. Fortunately, the *transverse mass* (M_T) of the $l\nu$ pair still provides significant discrimination between real and virtual W-decays (Rosner, 1989). The transverse mass is defined as the pseudo-invariant mass of the lepton and the neutrino constructed from the transverse components only :

$$M_T^2 \equiv (P_{T\nu} + P_{Tl})^2 - (\vec{P}_{T\nu} + \vec{P}_{Tl})^2 = 2P_{T\nu}P_{Tl}(1 - \cos\Delta\phi)$$

where $P_{T\nu}$ and P_{Tl} are the neutrino and lepton transverse momenta respectively, $\Delta\phi$ is the